SciPost Physics Submission

Spin-only dynamics of the multi-species nonreciprocal Dicke model

Joseph Jachinowski[1⋆] **and Peter B. Littlewood**[1,2†]

1 James Franck Institute and the Department of Physics, University of Chicago, Chicago, IL 60637, USA
2 School of Physics and Astronomy, University of St Andrews, St Andrews KY16 9AJ, UK

⋆ jachinowski@uchicago.edu , † littlewood@uchicago.edu

Abstract

The Hepp-Lieb-Dicke model is ubiquitous in cavity quantum electrodynamics, describing spin-cavity coupling which does not conserve excitation number. Coupling the closed spin-cavity system to an environment realizes the open Dicke model, and by tuning the structure of the environment or the system-environment coupling, interesting spin-only models can be engineered. In this work, we focus on a variation of the multi-species open Dicke model which realizes mediated nonreciprocal interactions between the spin species and, consequently, an interesting dynamical limit-cycle phase. In particular, we improve upon adiabatic elimination and, instead, employ a Redfield master equation in order to describe the effective dynamics of the spin-only system. We assess this approach at the mean-field level, comparing it both to adiabatic elimination and the full spin-cavity model, and find that the predictions are sensitive to the presence of single-particle incoherent decay. Additionally, we clarify the symmetries of the model and explore the dynamical limit-cycle phase in the case of explicit $\mathcal{PT}$-symmetry breaking, finding a region of phase coexistence terminating at an codimension-two exceptional point. Lastly, we go beyond mean-field theory by exact numerical diagonalization of the master equation, appealing to permutation symmetry in order to increase the size of accessible systems. We find signatures of phase transitions even for small system sizes.

Received Date
Accepted Date
Published Date

Contents

---

1 Introduction

At a microscopic level, the interactions between particles are inherently reciprocal as a consequence of Newton's third law; therefore, nonreciprocal interactions, interactions which generically violate Newton's third law, must be cleverly engineered to emerge [1]. This is done by allowing a system to interact reciprocally with a bath, then tracing out the bath degrees of freedom. If engineered properly, the resulting system dynamics may be characterized by effective nonreciprocal interactions which generically break time-reversal ($\mathcal{T}$) symmetry. A schematic depiction of this recipe is shown in Fig. 1. Although nonreciprocal interactions break time-reversal symmetry, the system may still separately possess a $\mathbb{Z}_2$ generalized parity ($\mathcal{P}$) symmetry or a combined parity-time ($\mathcal{PT}$) symmetry.

In manybody systems, nonreciprocal interactions between constituent particles can give rise to nonreciprocal phase transitions [2] in which a static phase is induced to rotate by tuning the balance of reciprocal and nonreciprocal interactions, thus establishing a dynamical limit-cycle phase explicitly or spontaneously breaking $\mathcal{PT}$-symmetry. Although not a necessary condition, nonreciprocal phase transitions are closely related to the appearance of exceptional points, constituting an "ultimate, unavoidable form of nonreciprocity" [2]. Realizing nonreciprocal phase transitions in quantum systems is physically challenging since the constituent particles are more microscopic and, in a loose sense, closer to the fundamental constraint of reciprocity in their interactions. Moreover, the definition of time-reversal symmetry in open quantum systems is subtle [3, 4] and the existence of exceptional points can change in different limits [5]. That being said, proposals have been introduced [6–8] to realize nonreciprocal phase transitions in quantum systems building off of previous work on the engineering of nonreciprocal interactions, most notably in the context of the non-Hermitian skin-effect [9, 10].

A paradigmatic quantum system with a $\mathbb{Z}_2$ parity symmetry is the Hepp-Lieb-Dicke model [11–13] describing the electric-dipole interaction between spin-1/2 particles and a single cavity mode of the electric field. This model is closely related to the Ising model (with all-to-all couplings) after eliminating the cavity degree of freedom [14, 15], perhaps the quintessential example of a model with a $\mathbb{Z}_2$ parity symmetry. In the context of the Dicke model, the symmetry-broken phase is called the superradiant phase (as opposed to the normal phase) and corresponds to a coherent, nonzero occupation of the cavity mode. A recent review of

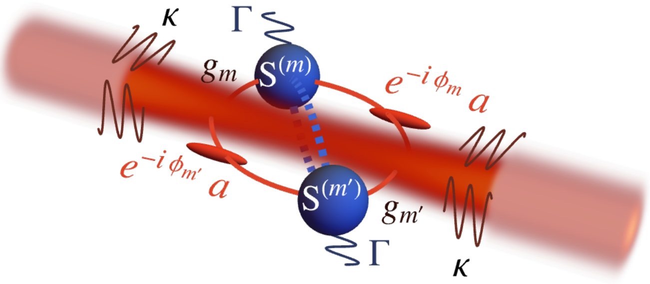

Figure 1: Schematic depiction of the system studied in this paper. A single cavity mode (dark red confocal Gaussian beam) coherent interacts with various species m and m' of collective spins (blue spheres) through phase shifted photons $e^{-i\phi_m}a$ and $e^{-i\phi_{m'}}a$ (red ellipsoids) with coupling strength g_m and $g_{m'}$. The cavity mode is coupled (dark red squiggles) to a bath of extra-cavity modes (pale red Gaussian beams) leading to effective dissipative dynamics of the cavity mode characterized by the decay rate κ. Similarly, the spins experience single-particle incoherent decay at the rate Γ. Upon tracing-out the cavity mode in addition to the bath modes, the spins of different species m and m' interact nonreciprocally (dashed blue lines), a result that is made possible by the well-defined phase relationship between the cavity photons interacting with the different species m and m'.

the Dicke model can be found in Ref. [16] including both equilibrium and driven-dissipative variations. For the rest of this paper, we focus on the dissipative Dicke model (without drive) and, therefore, drop the modifier.

A versatile platform which can realize the Dicke model is an atomic Bose-Einstein condensate (BECs) trapped in an optical cavity [17–20], where the superradiant phase transition is characterized as a process of self-organization and is related to the so-called "supersolid" phase transition [21]. One facet of the platform's versatility is the ability to introduce multiple spin species via spinor BECs. In this context, the Dicke model was recently extended to a nonreciprocal (or non-standard) two-species model [22], observed experimentally [23], and shown to exhibit a nonreciprocal phase transition to a dynamical limit-cycle phase [6] (referred to as the "dynamical phase" throughout this work, not to be confused with the "phases of a dynamical system" more broadly). While the existence of limit-cycle states or persistent oscillations has been observed in generalized Dicke models, for example, the states identified in Ref. [24] and Ref. [25] with reciprocal couplings only, the dynamical phase in the nonreciprocal Dicke model is induced by the nonreciprocity of the interactions.

In this work, we further investigate the model from Ref. [6], shown schematically in Fig. 1, deriving a Redfield master equation to describe the effective dynamics of the spin-only system, thus generalizing the analysis of Ref. [14] which considers a single-species reciprocal model. At the mean-field level–exact in the thermodynamic limit for the single-species Dicke model [26]–we compare the predictions of the full spin-cavity model, the spin-only model described by the Redfield quantum master equation, and the spin-only model obtained from adiabatic elimination of the cavity mode. We find that the spin-only model described by the Redfield master equation not only provides a better quantitative match to the full spin-cavity model, as expected, but also makes qualitatively different predictions from the adiabatic elimination model, principally in how it captures the effect of single-particle incoherent decay. Additionally, we further investigate the dynamical limit-cycle phase in the case of explicitly broken $\mathcal{PT}$-symmetry and uncover a region of phase-coexistence characterized by hysteresis terminating at a codimension-two exceptional point [27], consistent with the framework proposed in [2] for a model with explicitly broken $\mathcal{PT}$-symmetry. Lastly, we push beyond the mean-field theory analyzing the spin-only model in the low-number limit, finding signatures of the thermodynamic behavior in the steady-state density matrix and the spectrum of the Liouvillian.

The paper is organized as follows. In Sec. 2, we introduce the nonreciprocal Dicke model and describe the procedure to obtain the effective spin-only model by integrating out the photonic degrees of freedom resulting in the Redfield master equation Eq. 8. Additionally, we define the relevant symmetries of the open system at the level of the Liouvillian, clarifying the realization of $\mathcal{PT}$-symmetry in various limits. In Sec. 3, we analyze the model introduced in Sec. 2 at the mean-field level, exploring the phase diagram via the fixed-points, limit-cycles, and bifurcations of the corresponding nonlinear dynamical system. Our primary results for this section are summarized in Fig. 3 and Fig. 4 and discussed in Sec. 3.3 and Sec. 3.4. We conclude with Sec. 3.5 which discusses the model in the low-number limit. The superradiant phase is analyzed in Fig. 5 while the dynamical limit-cycle phase is analyzed in Fig. 6.

2 Description of the model

2.1 Description of the closed system

We study a quantum system consisting of three subsystems: spin (S), cavity (C), and bath (B) of extra-cavity modes. The total Hamiltonian has the general form

$$H = H_\mathrm{S} + H_\mathrm{SC} + H_\mathrm{C} + H_\mathrm{CB} + H_\mathrm{B} \tag{1}$$

where H_S, H_C, and H_B are noninteracting terms corresponding to the spin, cavity, and bath subsystems, respectively, H_SC is the interaction between the spins and the cavity, and H_CB is the interaction between the cavity and the bath. At this point, we assume that there is no direct interaction between the spins and the bath, although we will later insert dissipative spin terms by hand. The spin subsystem consists of spin-1/2 particles which are divided into distinguishable species m. The spin-up and spin-down states are separated by the energy ϵ. Motivated by the microscopic derivation of the model, see Appendix A, we take the species labels $m = -M, -M+1, \ldots, M-1, M$ where $M \geq 0$ is a fixed integer. While $2M+1$ is the total number of possible species, we let $M^\star$ denote the number of species with nonzero population N_m (and so at most $M^\star = 2M+1$). The case $M = 0$ and $M^\star = 1$ corresponds to the single-species model, while the case $M = 1$ and $M^\star = 2$ corresponds to a two-species model and will be the focus of this work. A spin j of species m is individually described by the vector spin-1/2 operator $\boldsymbol{s}^{(m,j)} = \left(s_1^{(m,j)}, s_2^{(m,j)}, s_3^{(m,j)}\right)$ with eigenvalues $\pm 1/2$ ($\hbar = 1$) for each component $i = 1$, 2, or 3. The cavity is described by a single bosonic mode of the electric field a of energy ω_c. Generically, we will assume that $\omega_c > 0$ microscopically corresponding to red-detuned pumping of the spins, see Appendix A, however interesting dynamical limit-cycle phases have also been investigated in the blue-detuned case [25,28]. The bath is described by a countable collection of bosonic extra-cavity modes of the electric field b_k of energy ξ_k. The noninteracting terms in the Hamiltonian are therefore ($\hbar = 1$)

$$H_\mathrm{S} = \epsilon \sum_{m=-M}^{M} S_3^{(m)} \tag{2}$$

$$H_\mathrm{C} = \omega_c a^\dagger a \tag{3}$$

$$H_\mathrm{B} = \sum_k \xi_k b_k^\dagger b_k \tag{4}$$

where $\boldsymbol{S}^{(m)} = \left(S_1^{(m)}, S_2^{(m)}, S_3^{(m)}\right) = \sum_{j=1}^{N_m} \boldsymbol{s}^{(m,j)}$ is the vector collective spin-($N_m/2$) operator defined for the N_m spin-1/2 particles of species m. The interactions between the subsystems are described by the terms ($\hbar = 1$)

$$H_{\text{SC}} = \sum_{m=-M}^{M} \frac{2g_m}{\sqrt{N_m}} S_1^{(m)} \left(e^{-i\phi_m} a + e^{i\phi_m} a^\dagger\right) \tag{5}$$

$$H_{\text{CB}} = \sum_k h_k \left(a^\dagger b_k + a b_k^\dagger\right) \tag{6}$$

where we take the couplings g_m and h_k to be real. The normalizing factor of $\sqrt{N_m}$ is introduced to ensure extensive scaling in the thermodynamic limit. The spin-cavity interaction H_{SC} includes counter-rotating terms essential to the Dicke model, while we assume only co-rotating terms are sufficient to describe the cavity-bath coupling in H_{CB} (i.e. making the rotating-wave approximation).

We impose conditions on the coupling strengths g_m and the phases ϕ_m which are motivated microscopically, see Appendix A for details. The coupling strengths are symmetric under swapping of species $m \longleftrightarrow -m$, $g_m = g_{-m}$ while the phases are anti-symmetric, $\phi_m = -\phi_{-m}$, necessitating $\phi_0 = 0$. Importantly, for a multi-species model $M^\star > 1$, the phase shift of the cavity mode cannot, in general, be removed via gauge transformation of the cavity or spin operators [29], a requirement for nonreciprocity [30].

2.2 Description of the open system with and without the cavity

The cavity-bath interaction H_{CB} is used to impose dissipative dynamics on the spin-cavity subsystem. In the standard treatment of cavity dissipation, we trace out the bath modes assuming zero temperature and a (continuous) flat spectral density or, equivalently, delta-function time-correlations. This assumption is valid for many finely spaced extra-cavity modes spanning a large spectral range with constant coupling strengths $h_k = h$. Doing so, we obtain the Gorini–Kossakowski–Sudarshan–Lindblad (GKSL) master equation for the density matrix [31] with quantum jump operator a at the rate κ. The adjoint GKSL master equation for a generic spin or cavity operator A follows as

$$\hat{\mathcal{L}}^* A = i\left[H_{\text{S}} + H_{\text{SC}} + H_{\text{C}}, A\right] + \kappa \hat{\mathcal{D}}^* [a] A + \Gamma \sum_{m=-M}^{M} \sum_{j=1}^{N_m} \hat{\mathcal{D}}^* \left[s_-^{(m,j)}\right] A \tag{7}$$

where $\hat{\mathcal{L}}^*$ is the adjoint Liouvillian (in this case Lindbladian) superoperator and $\hat{\mathcal{D}}^*[A]B = 2A^\dagger B A - \left\{A^\dagger A, B\right\}$ is the adjoint dissipation superoperator. We extract the time-evolution of correlation functions as $d\langle A\rangle/dt = \left\langle \hat{\mathcal{L}}^* A\right\rangle$ [32].

Single-particle incoherent decay is introduced phenomenologically with the quantum jump operator $s_-^{(m,j)} = s_1^{(m,j)} - i s_2^{(m,j)}$ at the rate Γ. This single-particle effect is not only essential to stabilizing the normal state when $\phi_m \neq 0$ [29, 33], as will be discussed in more depth later, but is also experimentally relevant. Moreover, it has been shown that single-particle incoherent decay can counter-act dephasing effects [34], restoring the superradiant transition in a single-species model. On the other hand, it violates the conservation of total spin which renders theoretical approaches such as Holstein-Primakoff expansions [16, 33] and coherent-state path integral approaches [35] inapplicable. Field theory approaches to the Dicke model with single-particle incoherent decay necessitate a somewhat more complicated treatment in terms of Majorana fermions [36]. Collective incoherent decay with quantum jump operator $S_-^{(m)}$ is sometimes studied [37, 38], but, unlike single-particle incoherent decay, it does not stabilize the normal state.

To obtain a description only in terms of the spins, we trace out the cavity mode in addition to the bath modes. The enlarged bath is now structured, and the previous assumption that the bath modes possess a flat spectral density is consistent with a Lorentzian spectral density of the cavity-bath eigenmodes. The time-correlations are, therefore, finite but exponentially suppressed [14] with the form $e^{-i\Delta\phi}e^{-i\omega_c t-\kappa|t|}$ where $\Delta\phi=\phi_m-\phi_{m'}$ encodes information on the relative phase of the spin-cavity interaction. We assume that the inverse decay rate $1/\kappa$ is sufficiently short compared to the time-scales of interest, allowing us to simplify the resulting master equation by extending the integration bound of the memory kernel. For details of the derivation, see Appendix B. Following this prescription, the adjoint Redfield master equation for a generic spin operator A is

$$\begin{aligned}\hat{\mathcal{L}}^*A=i\left[H_S,A\right]+i\sum_{m,m'=-M}^{M}\frac{g_m g_{m'}e^{-i\Delta\phi}}{\sqrt{N_m N_{m'}}}H^{\text{ind.}}_{jk}\left[\left(L_j^{(m)}\right)^\dagger L_k^{(m')},A\right]\\+\sum_{m,m'=-M}^{M}\frac{g_m g_{m'}e^{-i\Delta\phi}}{\sqrt{N_m N_{m'}}}D_{jk}\hat{\mathcal{D}}^*\left[L_k^{(m')},L_j^{(m)}\right]A+\Gamma\sum_{m=-M}^{M}\sum_{\ell=1}^{N_m}\hat{\mathcal{D}}^*\left[s_-^{(m,\ell)}\right]A\end{aligned}\tag{8}$$

where, again, $\hat{\mathcal{L}}^*$ is the adjoint Liouvillian superoperator, $L_1^{(m)}=S_-^{(m)}$ and $L_2^{(m)}=S_+^{(m)}$ are the quantum jump operators for each species m, and summation over the indices j and k is implied. The coefficient matrix $H^{\text{ind.}}$ of the coherent bath-induced Hamiltonian is

$$H^{\text{ind.}}=-\frac{1}{4}\begin{bmatrix}\frac{\omega_c-\epsilon}{\kappa^2+(\omega_c-\epsilon)^2} & \frac{\omega_c}{(\kappa+i\epsilon)^2+\omega_c^2}\\ \frac{\omega_c}{(\kappa-i\epsilon)^2+\omega_c^2} & \frac{\omega_c+\epsilon}{\kappa^2+(\omega_c+\epsilon)^2}\end{bmatrix}\tag{9a}$$

$$=-\frac{1}{16}\begin{bmatrix}\frac{1}{K_1}-\frac{1}{J_2} & \frac{1}{K_1}-\frac{i}{K_2}\\ \frac{1}{K_1}+\frac{i}{K_2} & \frac{1}{K_1}+\frac{1}{J_2}\end{bmatrix}\tag{9b}$$

while the bath-induced dissipator is expanded in terms of the generalized adjoint dissipation superoperator $\hat{\mathcal{D}}^*\left[A,B\right]C=2B^\dagger CA-\left\{B^\dagger A,C\right\}$ with off-diagonal rate-matrix

$$D=\frac{1}{4}\begin{bmatrix}\frac{\kappa}{\kappa^2+(\omega_c-\epsilon)^2} & \frac{\kappa+i\epsilon}{(\kappa+i\epsilon)^2+\omega_c^2}\\ \frac{\kappa-i\epsilon}{(\kappa-i\epsilon)^2+\omega_c^2} & \frac{\kappa}{\kappa^2+(\omega_c+\epsilon)^2}\end{bmatrix}\tag{10a}$$

$$=\frac{1}{16}\begin{bmatrix}\frac{1}{J_1}+\frac{1}{K_2} & \frac{1}{J_1}-\frac{i}{J_2}\\ \frac{1}{J_1}+\frac{i}{J_2} & \frac{1}{J_1}-\frac{1}{K_2}\end{bmatrix}\tag{10b}$$

Here, we have introduced the effective coupling parameters J_1, J_2, K_1, and K_2 which have units of energy and are given in terms of the system parameters κ, ω_c, and ϵ as

$$J_1=\frac{\Omega^4}{4\kappa\left(\kappa^2+\omega_c^2+\epsilon^2\right)}\tag{11a}$$

$$K_1=\frac{\Omega^4}{4\omega_c\left(\kappa^2+\omega_c^2-\epsilon^2\right)}\tag{11b}$$

$$J_2=\frac{\Omega^4}{4\epsilon\left(\kappa^2-\omega_c^2+\epsilon^2\right)}\tag{11c}$$

$$K_2=\frac{\Omega^4}{8\kappa\omega_c\epsilon}\tag{11d}$$

with the normalizing factor $\Omega^4=\left(\kappa^2+\omega_c^2\right)^2+2\left(\kappa^2-\omega_c^2\right)\epsilon^2+\epsilon^4$. Both matrices $H^{\text{ind.}}$ and D are then easily decomposed into a sum of Pauli matrices $(1,\sigma_1,\sigma_2,\sigma_3)$ as $H^{\text{ind.}}=(1/K_1)+$

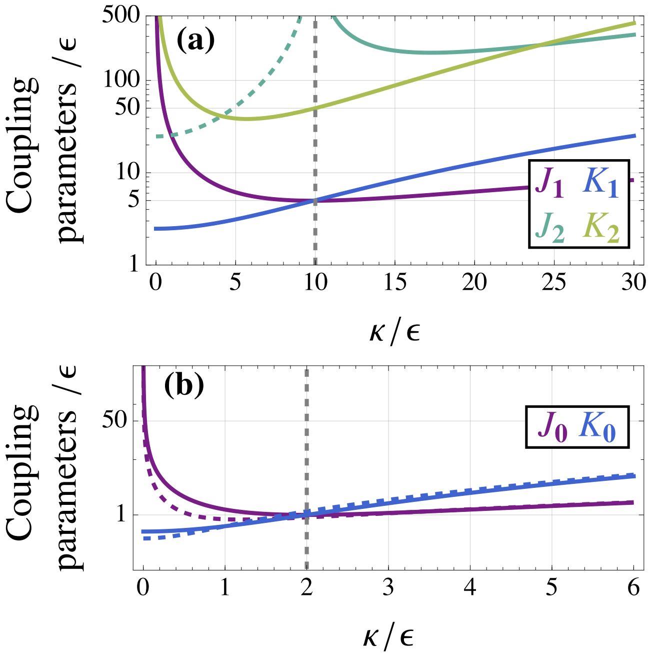

Figure 2: Effective coupling parameters in the spin-only system. (a) Coupling parameters J_1/ϵ, K_1/ϵ, J_2/ϵ, and K_2/ϵ from Eq. 8 as a function of the cavity decay rate κ/ϵ with the cavity energy $\omega_c/\epsilon = 10$ fixed (dashed gray line). For $\kappa^2 < \omega_c^2 - \epsilon^2$, J_2 is negative and, therefore, $-J_2$ is plotted in this region (dashed rather than solid turquoise). (b) Coupling parameters J_0/ϵ and K_0/ϵ from Eq. 12 in the fast-cavity limit $\kappa, \omega_c \gg \epsilon$ as a function of the cavity decay rate κ/ϵ with the cavity energy $\omega_c = 2\epsilon$ fixed (dashed gray line). The coupling parameters J_1/ϵ and K_1/ϵ (dashed purple and blue respectively) are compared to J_0/ϵ and K_0/ϵ using a smaller value of ω_c/ϵ in order to accentuate differences. There is no analogy to J_2/ϵ and K_2/ϵ in the system obtained from adiabatic elimination.

$(1/K_1)\sigma_1 + (1/K_2)\sigma_2 - (1/J_2)\sigma_3$ and $D = (1/J_1) + (1/J_1)\sigma_1 + (1/J_2)\sigma_2 + (1/K_2)\sigma_3$. The effective coupling parameters K_1 and K_2 are related to reciprocal interactions while J_1 and J_2 are related to nonreciprocal interactions. The time-evolution of correlation functions are similarly extracted as $d\langle A\rangle/dt = \left\langle \hat{\mathcal{L}}^* A\right\rangle$ [32]. We keep the bath-induced Hamiltonian which renormalizes the system Hamiltonian H_S, a practice which is not always necessary depending on the strength and spectral width of the bath [39], but is consistent with previous studies [14]. An alternative form of Eq. 8 is presented in Appendix B (see Eq. B.18) which makes clear the connection to the mean-field equations of motion, discussed later.

The strengths of the effective coupling parameters for a typical experimentally-realizable situation are shown in Fig. 2a. For the purposes of studying the mediated interactions between the spins, the system is often tuned to the fast-cavity limit $\kappa, \omega_c \gg \epsilon$. In this regime, there is a special point $\kappa = \omega_c$ where the coupling parameters satisfy $J_1 \approx K_1$ and $|J_2| \gg J_1$, K_1, and K_2 (so long as $\kappa = \omega_c$ is large enough), therefore resulting in coherent Hamiltonian interactions and dissipative interactions which are approximately equal in strength.

We stress that in deriving Eq. 8 we have not made the secular approximation. Including nonsecular terms breaks the complete-positivity (but not the Hermitian-preservation) of Eq. 8, indicated by the lack of a positive-semidefinite rate-matrix D, and can lead to unphysical results for the density matrix or correlation functions for certain initial conditions, specifically in the transient behavior [40]. Notwithstanding this point, including nonsecular terms correctly describes the known behavior of open Dicke models, in particular the superradiant transition [14], as well as the behavior of other multi-component systems interpolating from diagonal to off-diagonal (coherence between decay and pumping) dissipative processes [40].

Despite nonsecular terms, Eq. 8 can be brought into Lindblad form in the fast-cavity limit $\kappa, \omega_c \gg \epsilon$ [14]

$$\begin{aligned} \hat{\mathcal{L}}^* A = i\left[H_S, A\right] - i\frac{1}{4K_0}\sum_{m,m'=-M}^{M} \frac{g_m g_{m'} e^{-i\Delta\phi}}{\sqrt{N_m N_{m'}}}\left[S_1^{(m)} S_1^{(m')}, A\right] \\ + \frac{1}{4J_0}\sum_{m,m'=-M}^{M} \frac{g_m g_{m'} e^{-i\Delta\phi}}{\sqrt{N_m N_{m'}}} \hat{\mathcal{D}}^*\left[S_1^{(m')}, S_1^{(m)}\right] A + \Gamma \sum_{m=-M}^{M}\sum_{\ell=1}^{N_m} \hat{\mathcal{D}}^*\left[s_-^{(m,\ell)}\right] A \end{aligned} \tag{12}$$

where now $K_0 = \left(\kappa^2 + \omega_c^2\right)/4\omega_c$ and $J_0 = \left(\kappa^2 + \omega_c^2\right)/4\kappa$ are defined in analogy to the parameters K_1 and J_1; in particular, $K_1 \sim K_0$ and $J_1 \sim J_0$ in the fast-cavity limit $\kappa, \omega_c \gg \epsilon$, as shown in Fig. 2b. Neglecting the energy splitting ϵ allows the system to sample the bath at the same frequency, and the rate-matrix D, therefore, becomes constant.

2.3 Symmetries of the open system

Open quantum systems permit two distinct types of symmetries, weak (classical) and strong (quantum), distinguished by whether or not left and right symmetry-charges are separately conserved by the Liouvillian [32, 41]. In the case of strong symmetries, there exists a steady-state solution for the density matrix in each symmetry sector, whereas for a weak symmetry, the density matrix still generically approaches a unique steady-state. Here, the open system possesses weak symmetries only, and in the exact quantum treatment presented in Sec. 3.5 for finite system sizes, we find numerically that the density matrix approaches a unique steady-state. Although the continuous rotational symmetry of the spins has been broken, in the following section, we define two important $\mathbb{Z}_2$ symmetries.

The first $\mathbb{Z}_2$ symmetry arises due to parity conservation (in this case referring to even or odd) of the total excitation number, since the non-number-conserving counter-rotating terms in H_{SC} can only create or annihilate excitations in pairs. This is the relevant symmetry in the superradiant transition and, therefore, we refer to it as the "superradiant parity" (SR parity) symmetry going forward. Formally, the SR parity symmetry is a weak symmetry with respect to the parity operator $\Pi = e^{i\pi\sum_m S_3^{(m)}}$ for all forms of the Liouvillian: The Liouvillian in Lindblad form for the full spin-cavity model Eq. 7, the Liouvillian for the spin-only model described by the Redfield master equation Eq. 8, and the Liouvillian in Lindblad form for the spin-only model in the fast-cavity limit $\kappa, \omega_c \gg \epsilon$ Eq. 12.

The second $\mathbb{Z}_2$ symmetry provides a rule for interchanging species and gives rise to the nonreciprocal phase transition identified in Ref. [6]. For this reason, we refer to it as the "nonreciprocal parity-time" (NR $\mathcal{PT}$) symmetry going forward. The formal definition of the NR $\mathcal{PT}$-symmetry, however, is more subtle. For ease of explanation and transparent application in later sections, we restrict ourselves to a two-species model $M = 1$ and $M^\star = 2$ with balanced species populations $N_{-1} = N_1$ (and $N_0 = 0$).

First, we define the involutive bipartite parity operator $\mathbb{P}$ which swaps tensor product operators corresponding to the two species, i.e. $\mathbb{P}\left(A^{(-1)}B^{(1)}\right)\mathbb{P} = B^{(-1)}A^{(1)}$ for generic spin operators $A^{(-1)}$ and $B^{(1)}$ acting on the Hilbert spaces of species $m = -1$ and $m' = 1$, respectively. All forms of the Liouvillian (see above) at equal and opposite phases $\Delta\phi = \phi_1 - \phi_{-1} = 2\phi_1 \leftrightarrow -\Delta\phi = -(\phi_1 - \phi_{-1}) = -2\phi_1$ are related by the bipartite parity transformation $\mathbb{P}$. As a consequence, all forms of the Liouvillian have a weak symmetry with respect to $\mathbb{P}$ for phases $\Delta\phi = \phi_1 - \phi_{-1} = 2\phi_1 = k\pi$ with k an integer. In particular, for k odd, a gauge transformation brings Eq. 8 into the form of the standard two-species Dicke model, but may still exhibit interesting behavior resulting from the conservation of two collective spins and mixing of total-spin manifolds [42]. Additionally, Eq. 8 has a (modified) weak symmetry with respect to $\mathbb{P}$ for phases $\Delta\phi = \phi_1 - \phi_{-1} = 2\phi_1 = (k+1/2)\,\pi$ with k an integer since the factors $e^{-i\Delta\phi} = \pm i$ can be made equal after a gauge transformation of one of the two spin species, e.g. $e^{i\pi S_3^{(1)}} S_\pm^{(1)} e^{-i\pi S_3^{(1)}} = -S_\pm^{(1)}$. Tuning the phases ϕ_m can break and restore the weak symmetry with respect to $\mathbb{P}$ and, therefore, the phases ϕ_m can be thought of as a "chirality breaking" parameters [2].

Second, we provide a formal definition of time-reversal in open quantum systems. Inspired by the generalized $\mathcal{PT}$-symmetry discussed in Ref. [4], we define two similar involutive anti-unitary time-reversal operators $\mathbb{T}$ and $\mathbb{T}'$. The former performs Hermitian conjugation $\mathbb{T}A\mathbb{T} = A^\dagger$, while the latter performs complex conjugation $\mathbb{T}'A\mathbb{T}' = A^*$.

Lastly, the combined operators $\mathbb{PT}$ and $\mathbb{PT}'$ provide two different realizations of the NR $\mathcal{PT}$-symmetry. First, the operator $\mathbb{PT}'$ realizes a weak symmetry of the Liouvillian in Lindblad form for the full spin-cavity model Eq. 7 and the Liouvillian in Lindblad form for the spin-only model in the fast-cavity limit $\kappa, \omega_c \gg \epsilon$ Eq. 12. The Liouvillian for the spin-only model described by the Redfield master equation Eq. 8, however, does not exhibit the NR $\mathcal{PT}$-symmetry with respect to $\mathbb{PT}'$ since retaining the energy splitting ϵ means the system samples the bath at the slightly shifted frequencies. The lack of the NR $\mathcal{PT}$-symmetry with respect to $\mathbb{PT}'$, therefore, can be interpreted as resulting from the lack of Lindblad form. Second, upon removing single-particle incoherent decay $\Gamma = 0$, the operator $\mathbb{PT}$ realizes a weak symmetry of the Liouvillian in Lindblad form for the spin-only model in the fast-cavity limit $\kappa, \omega_c \gg \epsilon$ Eq. 12. In this case, the results of Ref. [43] under a Holstein-Primakoff approximation guarantee that the mean-field equations of motion, discussed later, possess a nonlinear $\mathcal{PT}$-symmetry. Reintroducing single-particle incoherent decay $\Gamma > 0$, however, explicitly breaks this realization of the NR $\mathcal{PT}$-symmetry with respect to the operator $\mathbb{PT}$ since there is no balancing single-particle incoherent pumping term; Eq. 12 is left with only the weaker NR $\mathcal{PT}$-symmetry with respect to the operator $\mathbb{PT}'$.

We note a final symmetry which will be important in Sec. 3.5. Since the spins are identically prepared and, in principal, not individual addressable, the system also has a weak permutation symmetry which formally arises from an $SU(4)$-symmetry of the Liouvillian superoperator [44, 45]. The symmetry is strong if there are no single-particle dissipative processes.

3 Analysis and results

3.1 Mean-field equations of motion

For the remainder of the paper, we focus on the spin-only system, although occasional comparison to the full spin-cavity system will prove helpful, for example to benchmark results.

We study the phases of the open system via the semiclassical equations of motion for the expectation values of the collective spin operators. Using Eq. 8, we compute the adjoint Redfield equation for the collective spin operators $S_j^{(m)}$. To obtain the mean-field theory, we take the expectation value and decouple all correlation functions, formally assuming that the second cumulants, equivalent to the second central moments, vanish. This assumption is exact in the thermodynamic limit $N_m \to \infty$. We introduce the normalized scalar parameters $\tau_j^{(m)} = \left\langle S_j^{(m)} \right\rangle / N_m$ for each species m. The result is a closed system of equations in $3 \times (2M+1)$ variables, excluding the cavity field. We write the equations compactly in terms of the total vector $\boldsymbol{\tau} = \left(\left(\tau_1^{(m)}\right), \left(\tau_2^{(m)}\right), \left(\tau_3^{(m)}\right)\right)$ organizing all species $-M, \ldots, M$ into $x = 1$, $y = 2$, and

$z = 3$ blocks. Then

$$\dot{\boldsymbol{\tau}} = \begin{bmatrix} \mathbf{0}_v \\ \mathbf{0}_v \\ -\Gamma \mathbf{1}_v \end{bmatrix} + \begin{bmatrix} -\Gamma \boldsymbol{I} & -\epsilon \boldsymbol{I} & \mathbf{0} \\ \epsilon \boldsymbol{I} + \boldsymbol{U}(\boldsymbol{\tau}_3) & -\Gamma \boldsymbol{I} + \boldsymbol{V}(\boldsymbol{\tau}_3) & \mathbf{0} \\ -\boldsymbol{U}(\boldsymbol{\tau}_2) & -\boldsymbol{V}(\boldsymbol{\tau}_2) & -2\Gamma \boldsymbol{I} \end{bmatrix} \boldsymbol{\tau} \tag{13}$$

where $\mathbf{0}_v$ and $\mathbf{1}_v$ are $(2M+1)$-component vectors of all zeros and ones, respectively, and $\mathbf{0}$ and $\boldsymbol{I}$ are the $(2M+1) \times (2M+1)$ zero and identity matrix, respectively. The quadratic nonlinearities are encoded in the $(2M+1)\times(2M+1)$ matrix-valued functions $\boldsymbol{U}$ and $\boldsymbol{V}$ which mix the species m and m'

$$U_{mm'}\left(\boldsymbol{\tau}_j\right) = 2\sqrt{\frac{N_{m'}}{N_m}} g_m g_{m'} \left(\frac{\cos\Delta\phi}{K_1} + \frac{\sin\Delta\phi}{J_1} \right) \tau_j^{(m)} \tag{14}$$

$$V_{mm'}\left(\boldsymbol{\tau}_j\right) = 2\sqrt{\frac{N_{m'}}{N_m}} g_m g_{m'} \left(\frac{\cos\Delta\phi}{K_2} + \frac{\sin\Delta\phi}{J_2} \right) \tau_j^{(m)} \tag{15}$$

In the thermodynamic limit $N_m \to \infty$, we neglect sub-extensive corrections to the energy ϵ and the single-particle incoherent decay rate Γ which are present in dynamical equations for finite-sized systems, see Appendix B for details. The phase-dependent coefficients in $\boldsymbol{U}$ and $\boldsymbol{V}$ are separated into reciprocal parts, expressed in terms of $\cos\Delta\phi$ which is an even function, and nonreciprocal parts, expressed in terms of $\sin\Delta\phi$ which is an odd function, with strengths characterized by the parameters K_1 and K_2 or J_1 and J_2, respectively. We stress that the coefficients J_1 and J_2 do not appear (or are infinite) in treatments of the reciprocal Dicke model [14]. We will mostly be concerned with the fast-cavity limit $\kappa, \omega_c \gg \epsilon$ and, in this case, we notice $\kappa = \omega_c$ yields a special point where J_2 is exceedingly large, as shown in Fig. 2a, therefore rendering the nonreciprocity described by $\boldsymbol{V}$ small.

The fixed-points $\dot{\boldsymbol{\tau}} = 0$ of Eq. 13 correspond to the roots of a $3\times(2M+1)$-order polynomial equation; although they are difficult to solve for in full generality, two immediate conclusions can be drawn. First, the x and y components of the spins are related as $-\Gamma\tau_1^{(m)} = \epsilon\tau_2^{(m)}$. Therefore, all steady-state solutions must lie in a plane defined by the normal $(\cos\beta, \sin\beta, 0)$ for each species with $\beta = \tan^{-1}(-\Gamma/\epsilon) + \pi/2$. Second, the incoherent, spin-down "normal state" solution $\boldsymbol{\tau}_{\text{ns}} = (\mathbf{0}_v, \mathbf{0}_v, (-1/2)\,\mathbf{1}_v)$ exists for all values of the system parameters.

We study the stability of the normal state fixed-point by expanding Eq. 13 to linear order in the deviation $\delta\boldsymbol{\tau} = \boldsymbol{\tau} - \boldsymbol{\tau}_{\text{ns}}$ to obtain

$$\delta\dot{\boldsymbol{\tau}} = \begin{bmatrix} -\Gamma \boldsymbol{I} & -\epsilon \boldsymbol{I} & \mathbf{0} \\ \epsilon \boldsymbol{I} + \boldsymbol{U}(-1/2) & -\Gamma \boldsymbol{I} + \boldsymbol{V}(-1/2) & \mathbf{0} \\ \mathbf{0} & \mathbf{0} & -2\Gamma \boldsymbol{I} \end{bmatrix} \delta\boldsymbol{\tau} \tag{16}$$

The equations for the z-components of each species m decouple and are solved by simple exponential decay $\delta\tau_3^{(m)}(t) \propto e^{-2\Gamma t}$. They do not affect the stability of the normal state fixed-point and, therefore, we can exclude them from our analysis. The eigenvalues of the reduced $2(2M+1)\times 2(2M+1)$ matrix are obtained from the characteristic polynomial, which can be further reduced to a $(2M+1)$-order polynomial by Schur's formula.

3.2 Comparison to semiclassical adiabatic elimination

We compare the mean-field dynamical system Eq. 13 resulting from formally tracing out the cavity and extra-cavity modes with the system of equations obtained via adiabatic elimination of the spin-cavity system at the semiclassical level. Semiclassical adiabatic elimination proceeds as follows. Starting from Eq. 7, we compute not only the adjoint GKSL equation for the collective spin operators $S_j^{(m)}$ but also for the cavity mode a. Then we obtain the mean-field dynamical system similarly to before, introducing an additional scalar parameter for the cavity mode $\alpha = \langle a \rangle$. Demanding that the cavity stay in the steady-state $\dot{\alpha} = 0$, we can express α in terms of spin parameters only with the equations of motion depending on the real combination

$$e^{-i\phi_m}\alpha + e^{i\phi_m}\alpha^* = -\frac{1}{2}\sum_{m=-M}^{M}\frac{g_m}{\sqrt{N_m}}\left(\frac{\cos\Delta\phi}{K_0} + \frac{\sin\Delta\phi}{J_0}\right)\tau_1^{(m)} \tag{17}$$

Substitution of Eq. 17 leads to a system of equations similar to Eq. 13

$$\dot{\boldsymbol{\tau}} = \begin{bmatrix} \mathbf{0}_v \\ \mathbf{0}_v \\ -\Gamma\mathbf{1}_v \end{bmatrix} + \begin{bmatrix} -\Gamma\boldsymbol{I} & -\epsilon\boldsymbol{I} & \mathbf{0} \\ \epsilon\boldsymbol{I} + \boldsymbol{W}(\boldsymbol{\tau}_3) & -\Gamma\boldsymbol{I} & \mathbf{0} \\ -\boldsymbol{W}(\boldsymbol{\tau}_2) & \mathbf{0} & -2\Gamma\boldsymbol{I} \end{bmatrix}\boldsymbol{\tau} \tag{18}$$

where the quadratic nonlinearities are now encoded in the $(2M+1)\times(2M+1)$ matrix-valued function $\boldsymbol{W}$

$$W_{mm'}\left(\tau_j\right) = 2\sqrt{\frac{N_{m'}}{N_m}}g_m g_{m'}\left(\frac{\cos\Delta\phi}{K_0} + \frac{\sin\Delta\phi}{J_0}\right)\tau_j^{(m)} \tag{19}$$

The semiclassical adiabatic elimination procedure yields identical results to starting from Eq. 12 rather than Eq. 8. In particular, we highlight the absence of the y-z quadratic nonlinearities in the y-equations and the y-y quadratic nonlinearities in the z-equation, i.e. there is no analogy to the matrix-valued function $\boldsymbol{V}$. This result is consistent with the fast-cavity limit $\kappa, \omega_c \gg \epsilon$ of Eq. 13.

Similar to Eq. 16, the linearization of Eq. 18 is

$$\delta\dot{\boldsymbol{\tau}} = \begin{bmatrix} -\Gamma\boldsymbol{I} & -\epsilon\boldsymbol{I} & \mathbf{0} \\ \epsilon\boldsymbol{I} + \boldsymbol{W}(-1/2) & -\Gamma\boldsymbol{I} & \mathbf{0} \\ \mathbf{0} & \mathbf{0} & -2\Gamma\boldsymbol{I} \end{bmatrix}\delta\boldsymbol{\tau} \tag{20}$$

The structural differences of Eq. 16 and Eq. 20 are not particularly profound in the single-species case; the linear stability analysis predicts the same stability and bifurcations, albeit at slightly shifted positions due to renormalization of the rates. However, in the following section, we show that the linear stability analysis fails to predict the correct stability of the normal state fixed-point in a multi-species model $M^\star > 0$ due to small but nonzero couplings between different species m which are exactly zero in the adiabatic elimination model.

3.3 Comparison of mean-field phase diagrams

The phase diagrams of single-species models have been investigated in much detail, including supplemental interaction terms and dissipative processes. Some aspects of the single-species models generalize to the multi-species nonreciprocal model considered in this paper. We start from the normal phase which is characterized by the stability of the normal state fixed-point $\boldsymbol{\tau}_{\text{ns}}$. First, the steady-state superradiant phase transition results from a supercritical pitchfork bifurcation of the dynamical system Eq. 13 and is marked by the determinant of the linear stability analysis of the normal state fixed-point $\boldsymbol{\tau}_{\text{ns}}$ vanishing (for the quantum jump operators considered here [34]). Secondly, there exists regions of phase coexistence characterized by multiple linearly stable fixed-points with complementary basins of attraction [46, 47]. And lastly, we find stable limit-cycle states [6, 23, 29, 33] constituting a dynamical phase.

To illustrate some of these features, we focus on the two-species model and set the parameters $g = g_1 = g_{-1}$ and $\phi = \phi_1 = -\phi_{-1}$. Overall, the dynamical system Eq. 13 produces a phase diagram in terms of the number of stable fixed-point solutions very similar to that presented in Ref. [6], employing adiabatic elimination as in Eq. 18. In the following section, however, we compare the predictions both qualitatively and quantitatively. Then we discuss details of the dynamical limit-cycle phase in Sec. 3.4.

The symmetries discussed in Sec. 2.3 result in symmetries of the dynamical systems Eq. 13 and Eq. 18. Specifically, the SR parity symmetry is realized as $\left(\tau_1^{(m)},\tau_2^{(m)}\right)\longleftrightarrow-\left(\tau_1^{(m)},\tau_2^{(m)}\right)$. The NR $\mathcal{PT}$-symmetry with respect to $\mathbb{PT}'$ does not lead to a natural $\mathcal{PT}$-symmetry of the dynamical systems. Therefore, we interpret our results as well as those of Ref. [6] as pertaining to explicitly broken NR $\mathcal{PT}$-symmetry at the mean-field level. Instead, we focus on the bipartite parity transformation which is realized as $\left(\phi,\boldsymbol{\tau}^{(m)}\right)\longleftrightarrow\left(-\phi,\boldsymbol{\tau}^{(-m)}\right)$. The bipartite parity transformation involves the parameter ϕ and so the symmetry-broken solution pairs exist at different points in parameter space. We note that, without single-particle incoherent decay $\Gamma=0$, the NR $\mathcal{PT}$-symmetry with respect to $\mathbb{PT}$ of the Liouvillian in Lindblad form for the spin-only model in the fast-cavity limit $\kappa,\omega_c\gg\epsilon$ *does* yield a $\mathcal{PT}$-symmetry of the dynamical systems, namely $t\to-t$ and $\tau_1\to-\tau_1$ or $\tau_2\to-\tau_2$, flipping the chirality while leaving the quantization axis τ_3 invariant.

The critical coupling strength for the transition from the normal phase to the superradiant phase can be calculated analytically. In the single-species case, this reproduces the well-known critical coupling strength [16]

$$g_c^{(1)}\to\sqrt{\frac{\left(\kappa^2+\omega_c^2\right)\left(\Gamma^2+\epsilon^2\right)}{4\omega_c\epsilon}}\tag{21}$$

in the fast-cavity limit $\kappa,\omega_c\gg\epsilon$. In the two-species case, we find

$$g_c^{(2)}=\sqrt{\frac{\Gamma^2+\epsilon^2}{\left(\epsilon/K_1-\Gamma/K_2\right)}\frac{1}{f\left(\phi\right)}\left(1\pm\sqrt{1-f\left(\phi\right)}\right)}\tag{22}$$

where the dependence on the phase ϕ is described by the function

$$f\left(\phi\right)=\left(1+\left(\frac{\epsilon/J_1-\Gamma/J_2}{\epsilon/K_1-\Gamma/K_2}\right)^2\right)\sin^2\left(2\phi\right)\tag{23}$$

This result is consistent with the critical coupling strength originally reported in Ref. [22], expressed in terms of experimentally relevant parameters, up to renormalization corrections found here. The critical coupling strength $g_c^{(2)}$ may have two, one, or zero solutions, as shown in Fig. 3. When it exists, the smaller solution ("−", lower branch in Fig. 3) indicates the transition from the normal phase to the superradiant phase. The larger solution ("+", upper branch in Fig. 3), though very close to indicating the emergence of new (unstable) fixed-point solutions, only provides local information on the stability of the normal state fixed-point $\boldsymbol{\tau}_{\mathrm{ns}}$. In the fast-cavity limit $\kappa,\omega_c\gg\epsilon$, we can express the critical coupling strength for the two-species model $g_c^{(2)}$ in terms of the critical coupling strength for the single-species model $g_c^{(1)}$ presented earlier

$$g_c^{(2)}\to g_c^{(1)}\sqrt{\frac{1}{\tilde{f}\left(\phi\right)}\left(1\pm\sqrt{1-\tilde{f}\left(\phi\right)}\right)}\tag{24}$$

where the function f has been adjusted to $\tilde{f}\left(\phi\right)=\left(1+\left(\omega_c/\kappa\right)^2\right)\sin^2\left(\phi\right)$. The expressions Eq. 22 and Eq. 24 are compared in Fig. 3a to the prediction following from Eq. 7 which retains the cavity mode. The expression Eq. 22 is always closer to the prediction with the cavity mode, although there are significant deviations even in the fast-cavity limit $\kappa,\omega_c\gg\epsilon$. The expressions, however, are all very close for $\omega_c\approx\kappa$, the point discussed previously at which the coherent Hamiltonian interactions and dissipative interactions are approximately equal in strength.

The argument above, however, ignores the possibility of the normal state fixed-point $\boldsymbol{\tau}_{\text{ns}}$ loosing stability via a different mechanism. In fact, even for $\omega_c = \kappa$ where the critical coupling strengths $g_c^{(2)}$ calculated in different limits quantitatively agree, the linear stability analyses of the normal state fixed-point Eq. 16 and Eq. 20 can produce different results, as shown in Fig. 3b and c. In particular, the transition from the normal phase to the dynamical limit-cycle phase indicated by a supercritical Hopf bifurcation, see Fig. 4, is modified. In the limit of vanishing single-particle incoherent decay rate $\Gamma \to 0$, the linear instability of the normal state fixed-point $\boldsymbol{\tau}_{\text{ns}}$ swells to wash-out the normal phase for all nonzero values of the coupling strength g and phase ϕ [33], as shown in the inset of Fig. 3b for a cross-section. This features is correctly predicted by Eq. 16 while Eq. 20 predicts the persistence of the normal phase, as shown in the inset of Fig. 3c for a cross-section. Inclusion of single-particle incoherent decay enables transition to the dynamical phase at finite coupling strength g and phase ϕ. Additionally, we note that Eq. 16 predicts the appearance of a codimension-two fold-Hopf bifurcation along the trajectory in Fig. 3b from the normal phase to the dark-purple region, a feature which does not occur in Fig. 3c as predicted by Eq. 20. However, since the system still flows to the superradiant fixed-points past the transition, this feature does not affect the long-time dynamics.

3.4 Features of the dynamical limit-cycle phase

Perhaps the most striking feature of the model is the appearance of a dynamical limit-cycle phase. Since the NR $\mathcal{PT}$-symmetry is explicitly broken, the transition from the normal phase to the dynamical phase for $\phi \neq \pi/4$ deterministically selects a $\mathcal{PT}$-broken limit-cycle state, as shown in Fig. 4a and b for $\phi = \pi/4 - 0.1$. The limit-cycle state grows continuously from the normal state fixed-point, despite the lack of spontaneous symmetry breaking [48]. There are still small differences in the limit-cycle state, even when the single-particle incoherent decay rate is large enough such that Eq. 16 and Eq. 20 produce qualitatively identical and quantitatively close predictions for the stability of the normal state fixed-point $\boldsymbol{\tau}_{\text{ns}}$, e.g. $\Gamma \gtrsim 8 \times 10^{-3}$ for the parameters used in Fig. 3b and c. While Eq. 13 and Eq. 18 predict nearly identical oscillation frequencies of the limit-cycle (bottom panel of Fig. 4a), discontinuously jumping to a nonzero value as a result of the Hopf bifurcation, the precise shapes of the limit-cycle states differ as indicated by the differences in the time-averaged “magnetization” $\left\langle \tau_3^{(m)}(t) \right\rangle$ (top panel of Fig. 4a) as well as the time-averaged oscillation radius $\left\langle \sqrt{\left(\tau_1^{(m)}(t)\right)^2 + \left(\tau_2^{(m)}(t)\right)^2} \right\rangle$ (middle panel of Fig. 4a). Qualitatively, the limit-cycles are very similar, as shown in Fig. 4b.

Along the line $\phi = \pi/4$ bipartite parity symmetry is restored, as shown in Fig. 4c and d (top row), bisecting regions with bipartite parity symmetry-broken limit-cycle states. As the strength of the nonreciprocity is increased via the coupling strength g along the line $\phi = \pi/4$, we find numerical evidence for a codimension-two exceptional point, as described in Ref. [2], where principally the parity-symmetric limit-cycle state loses stability, replaced by coexistence between two stable parity-broken limit-cycle states. We identify the coexistence region by the appearance of hysteresis, as shown in Fig. 4e. In a small region of phases about $\phi = \pi/4$, growing for increasing coupling strength g, whether the system is initialized with a symmetric (solid) or anti-symmetric (dashed) perturbation from the normal state fixed-point $\boldsymbol{\tau}_{\text{ns}}$ effects which limit-cycle state it converge to in the long-time limit. Lastly, as the coupling straighten g is increased even more near $\phi = \pi/4$, we find dynamics which appear chaotic, as noted in Ref. [6], before the appearance of new stable fixed-points which ultimately eliminate the dynamical phase.

3.5 Exact quantum approach

Despite the power of mean-field approaches applied to the Dicke model, away from the thermodynamic limit the mean-field approach is expected to fail. In order to investigate systems with low particle numbers, we instead exactly solve the quantum master equation $\dot{\rho} = \hat{\mathcal{L}}\rho$ numerically, an approach which is tractable due to the elimination of the cavity mode and the exploitation of permutation symmetry. Steady-states of the density matrix solve the simpler equation $\hat{\mathcal{L}}\rho_{\text{ss}} = 0$ and, similarly to mean-field theory, define the phase of the system. First- and second-order phase transitions are, therefore, connected to non-analytic changes in ρ_{ss} in the thermodynamic limit and are indicated by closing of the Liouvillian gap, defined later [49]. In the fast-cavity limit $\kappa, \omega_c \gg \epsilon$, we use the Liouvillian in Lindblad form Eq. 12. Although for a single-species model, the steady-state is the completely mixed state $\rho \propto 1$ as a result of Hermitian quantum jump operators [14], the multi-species model still hosts nontrivial steady-states.

The weak permutation symmetry allows us to decompose the density matrix as

$$\rho = \sum_{(s_{-M},\dots,s_M)} p_{(s_{-M},\dots,s_M)}\rho_{(s_{-M},\dots,s_M)} \tag{25}$$

where $p_{(s_{-M},\dots,\sigma_M)}$ is the probability of density matrix block $\rho_{(s_{-M},\dots,s_M)}$, and s_m run over the allowed spins of each species m (not to be confused with the individual spin operators $\boldsymbol{s}^{(m,j)}$) [50]. That is, there is no coherence between different spin manifolds $(s_{-M},\dots,s_M)$, even though single-particle dissipative processes break the total spin conservation. While the dimension of the Hilbert space naively scales exponentially with particle number, $\mathcal{O}\left(4^N\right)$ for a single species, permutation symmetry and the assumption of a permutation-symmetric initial condition restricts the dynamics of the density matrix to the symmetric subspace of the Hilbert space with a dimension that scales polynomially with particle number, $\mathcal{O}\left(N^3\right)$ or even $\mathcal{O}\left(N^2\right)$ for a single species when only diagonal processes (decay and pumping with no coherence) are included [51]. The reduction in the dimension leads to speed-up of numerical calculations such as finding the spectra, steady-states, or complete time-resolved dynamics. For multi-species models, however, the scaling is less powerful, going as $\mathcal{O}\left(N^{3M^\star}\right)$ in general, i.e. $\mathcal{O}\left(N^6\right)$ for the two-species model considered here. In practice, this allows us to simulate two-species systems with up to 7 particles in each species (roughly the equivalent to a single-species system with 42 particles), enough to resolve distinct features of the steady-states and phases but not enough to investigate finite-size scaling and the connection to the classical limit.

To help visualize the density matrix, we first calculate the reduced density matrix for each species $\rho^{(m)}$, then calculate the Wigner (quasi-probability) distribution $W^{(m)}_{s_m}(\vartheta, \varphi)$ defined on the sphere parameterized by the polar angle ϑ and the azimuthal angle φ [52] for each allowed value of the spin s_m, and lastly calculate the spin-average Wigner distribution $W^{(m)}(\vartheta, \varphi)$, see Appendix C for details.

With this approach, we analyze the effect of nonreciprocity characterized by the phase ϕ on the superradiant state in the two-species model at the mean-field level and in a quantum system with 6 particles in each species. The results are shown in Fig. 5. For $\phi \approx 0$, the steady-states of species 1 ($m = +1$) and 2 ($m = -1$) are nearly identical. At the mean-field level, there exists two fixed-point attractors with nonzero values of $\tau_3^{(m)}$ respecting the SR parity symmetry, and the locations of the fixed-point attractors in the coordinates of species 1 and 2 are approximately equivalent. In the quantum system, the spin-averaged Wigner distribution exhibits resolved peaks at $\varphi = \tan^{-1}(-\Gamma/\epsilon)$ and $\tan^{-1}(-\Gamma/\epsilon) + \pi$, very close to $\varphi = 0$ and π since $\Gamma \ll \epsilon$. The small system size reduces the contrast of the superradiant state from the normal state centered at the south pole $\vartheta = \pi$ (not shown). As the nonreciprocity is increased through the phase ϕ, the locations of the fixed-point attractors in the coordinates of species 1 and 2 differentiate, with species 1 moving away from the origin and species 2 moving towards the origin. In turn, the peaks in the spin-averaged Wigner distribution of species 1 increase in contrast slightly, while the peaks in the spin-averaged Wigner distribution of species 2 decreases in contrast approaching the constant value $W^{(m)}(\vartheta, \varphi) \approx 1/4\pi$ associated with the completely mixed state $\rho^{(m)} \propto 1^{(m)}$, but not fully losing resolution of the superradiant peaks. Note for $\phi \to -\phi$, we find gain in contrast in species 2 and loss of contrast in species 1, as expected by bipartite parity transformation. Finally, as the phase $\phi \to \pi/4$, we observe the peaks of species 1 also decreases in contrast as bipartite parity symmetry is restored.

Lastly, we identify signatures of the dynamical state in the quantum system by analyzing the Liouvillian spectrum, eigenmatrices corresponding to slow, spiraling decay, as well as the Liouvillian gap. In Fig. 6a, an example of the Liouvillian spectrum within the mean-field dynamical limit-cycle phase is shown for a system with 6 particles in each species. The zero-eigenvalue $\lambda_0 = 0$ corresponds to the steady-state density matrix. The Liouvillian eigenvalue with the smallest nonzero real-part in magnitude is λ_1 (λ_1^*), and the corresponding eigenmatrix decays at the slowest possible rate $\Re(\lambda_1)$ and induces coherences which oscillate at the frequency $\Im(\lambda_1)$. The spin-averaged Wigner distribution of the reduced eigenmatrix for species 1 ($m = +1$) corresponding to eigenvalue λ_1 is shown in Fig. 6b. We find a (negative) concentration of quasi-probability around the latitude of the mean-field limit-cycle state. The large width of the band is due to the small system size.

The Liouvillian gap Δ is defined as $\Delta = -\Re(\lambda_1)$ [49]. It has been argued that the appearance of limit-cycle states in the thermodynamic limit correspond to the simultaneous closing of the Liouvillian gap by a set of eigenvalues coming in complex conjugate pairs and equally spaced in their imaginary-part [53]. While large systems sizes are currently inaccessible in our approach, we investigate the Liouvillian gap Δ as a function of the coupling strength g near the mean-field phase transition from the normal phase to the dynamical limit-cycle phase for 2 particles in each species up to 6 particles in each species, as shown in Fig. 6c setting the phase $\phi = \pi/4$. The Liouvillian gap begins to decrease as the system size increases, close to the mean-field Hopf bifurcation in the thermodynamic limit. However, as shown in Fig. 6a, it is difficult to ascertain if the eigenvalues with larger imaginary part are approaching the imaginary axis with the proposed parabolic envelope [53].

4 Conclusion

In this work, we have developed and analyzed an effective spin-only description of the multi-species nonreciprocal Dicke model based on the Redfield master equation which improves upon semiclassical adiabatic elimination procedures. Through a mean-field analysis, we have demonstrated that this approach not only provides better quantitative agreement with the full spin-cavity model but also captures crucial qualitative features. Additionally, we have explored various symmetries of the effective model and, in the case of explicitly broken $\mathcal{PT}$-symmetry, uncovered a region of phase coexistence between parity symmetry-broken limit-cycle states terminating at an exceptional point. Furthermore, eliminating the cavity mode and leveraging the model's underlying permutation symmetry enabled us to probe the exact dynamics of the density matrix for system sizes larger than would otherwise be feasible. This analysis revealed that signatures of macroscopic phases, including both the superradiant phase and the onset of dynamical instabilities leading to limit-cycles states at the mean-field level, are detectable in small systems. In future work, the fine-grained phases within the region of phase coexistence could be explored, as well as the transition to chaos. Additionally, expanding the accessible system size could help connect the quantum and classical limits in a multi-species model.

5 Acknowledgments

The authors acknowledge useful discussions with Jonathan Keeling. JJ acknowledges useful discussion with Matteo Brunelli, Tobias Nadolny, and Michel Fruchart.

Funding information PBL is partially supported by the Moore Foundation grant GBMF12763. This research benefited from the Physics Frontier Center for Living Systems funded by the National Science Foundation (PHY-2317138).

A Microscopic parameters

In this section of the appendix, we describe the experimental system motivating the model described in the main text.

We consider a system of atoms of mass m_a interacting with high-frequency electric fields and a uniform bias magnetic field. In particular, the electric field is comprised of two components: a monochromatic classical "pump" field of frequency ω_p and a monochromatic quantum field of frequency ω_c' (different from the ω_c in the main text). The pump field consists of a single macroscopically occupied spatial-polarization mode labeled by the wavevector $\boldsymbol{k}_p$ and polarization $\boldsymbol{\varepsilon}_p$. The quantum field consists of a single spatial mode labeled by the wavevector $\boldsymbol{k}_c$ and two orthonormal polarization modes $\boldsymbol{\varepsilon}_c^{(j)}$ for $j = 1, 2$, since we have not assumed either to be macroscopically occupied. Finally, the classical pump field and quantum field are retro-reflected by mirrors to form standing waves termed the optical lattice and the cavity mode, respectively. The optical lattice has Bloch eigenstates $|n, q\rangle$ where n is the band-index and q is the quasimomentum. For simplicity, we choose the optical lattice to be aligned with the z-axis, $\boldsymbol{k}_p \propto \hat{\boldsymbol{z}}$.

If we assume that the electric field is far-detuned from any electronic (optical) transitions in the atoms and that the intensity is sufficiently low to limit saturation effects, then the atom-field interaction is effectively governed by the dynamics of the magnetic sublevels coupled to the polarization modes of the field and is modeled by the interaction [54]

$$V_d = \sum_{j,k} E_j^{(+)} \alpha_{jk} E_k^{(-)} \tag{A.1}$$

where $E_j^{(\pm)}$ denotes the right-handed (+) and left-handed (−) frequency components of the j-th spatial component of the electric field $\boldsymbol{E}$. The subscript d indicates that the interaction is derived in the electric dipole approximation. The operator α_{jk} is known as the polarizability tensor and can be separated into scalar, vector, and tensor parts

$$\alpha_{jk} = \alpha_{jk}^{(s)} + \alpha_{jk}^{(v)} + \alpha_{jk}^{(t)} \tag{A.2}$$

$$\alpha_{jk}^{(s)} = \alpha_s \delta_{jk} \tag{A.3}$$

$$\alpha_{jk}^{(v)} = -i \frac{\alpha_v}{2f} \sum_{\ell} \epsilon_{jk\ell} f_\ell \tag{A.4}$$

$$\alpha_{jk}^{(t)} = \frac{\alpha_t}{2f\,(2f-1)} \left(3\left(f_j f_k + f_k f_j\right) - 2\boldsymbol{f}^2 \delta_{jk}\right) \tag{A.5}$$

where the coefficients α_s, α_v, and α_t are the conventional scalar, vector, and tensor polarizabilities defined in Ref. [55], f is the hyperfine angular momentum of the atoms in the electronic ground state, and f_ℓ are the associated x, y, and z components of the spin-f operators. In the main text, we set $M = f$. The polarizabilities are strong functions of frequency and exhibit resonance behavior. Therefore, although the hierarchy $|\alpha_s| > |\alpha_v| > |\alpha_t|$ may seem natural, it does not always hold. For example, in Cs, the scalar polarizability vanishes at $\lambda = 880.2$ nm between the D1 and D2 transitions while the vector polarizability remains appreciable [55]. This behavior may be an asset for experiments rather than a liability, allowing for dramatic tuning of the ratio α_v/α_s which is a primary parameter in the Dicke model derived later.

We consider the case of bosonic atoms (f even) at low temperature, and assume the atoms form a Bose-Einstein condensate (BEC) in the zero-quasimomentum state $q = 0$ of the ground band $n = 0$ of the optical lattice. However, the optical lattice potential couples the BEC to the edges of the first Brillouin zone via Bragg transitions. Imposing orthogonality of the optical latices and cavity mode $\boldsymbol{k}_p \cdot \boldsymbol{k}_c = 0$ and neglecting transitions between the ground and excited bands assuming a large enough intensity of the pump field, we can construct a two-mode model in momentum-space. Moreover, if we assume a large enough uniform bias magnetic field $|\boldsymbol{B}|$ in the direction of the pump field $\boldsymbol{B} \parallel \boldsymbol{k}_p$, then we can neglect spin-exchange processes. This assumption ensures that the model is diagonal in the magnetic quantum number m and that only one polarization mode of the cavity $\boldsymbol{\varepsilon}_c^{(1)}$ is coupled to the BEC.

Overall, we obtain the Dicke model presented in the main text in the rotating frame of the pump field with the parameters given microscopically as

$$\epsilon = E_L\left(k_p\right) - E_L\left(0\right) + \frac{k_c^2}{2m_a} - \omega_p \tag{A.6}$$

$$\omega_c = \omega_c' - \omega_p + 2\left|E_c\right|^2 N_m \sum_{m=-f}^{f}\left(\alpha_s + \frac{\alpha_t\left(f\left(f+1\right) - 3m^2\right)}{2f\left(2f-1\right)}\right) \tag{A.7}$$

$$G_m = 2\sqrt{2}\nu E_p E_c\left(\alpha_s\cos\left(\varphi\right) - i\frac{\alpha_v}{2f}\sin\left(\varphi\right)e^{-i\chi}m + \frac{\alpha_t\left(f\left(f+1\right) - 3m^2\right)}{2f\left(2f-1\right)}\cos\left(\varphi\right)\right) \tag{A.8}$$

The energy splitting ϵ depends on the difference in eigenenergies between the Bloch state at the edge of the Brillouin zone $E_L\left(k_p\right)$ and the zero-quasimomentum state $E_L\left(0\right)$, the recoil energy of the cavity mode $k_c^2/2m_a$, and and the energy of the pump field $\omega_p = k_p c$. The energy of the cavity mode ω_c is mostly given by the bare energy of the cavity mode ω_c' relative to the energy of the pump field ω_p, but also includes a correction due to the presence of the BEC with strength proportional to the atom number N_m, where $E_c = \sqrt{\hbar\omega_c'/2\epsilon_0 V}$ is the amplitude normalization of the quantized electromagnetic field (ϵ_0 is the permittivity of free space and V is the quantization volume). Finally, G_m is the complex coupling of the two-level systems in momentum-space to the cavity mode. The coupling depends on the macroscopic amplitude of the pump field E_p (which we have chosen to be real by imposing a phase reference), the amplitude normalization of the quantized electromagnetic field E_c, as well as an overlap integral ν between the potential term $\cos\left(k_p z\right)$, the Bloch state at the edge of the Brillouin zone $\left\langle 0, k_p\right|$, and the zero-quasimomentum state $|0,0\rangle$. The polarization of the pump field is described by the parameters φ and χ as $\boldsymbol{\varepsilon}_p = \left(\sin\left(\varphi\right)e^{i\chi}, \cos\left(\varphi\right), 0\right)$. If we assume without loss of generality that the cavity mode is aligned with the x-axis, $\boldsymbol{k}_c \propto \hat{\boldsymbol{x}}$, then φ gives the angle of linear polarization relative to the y-axis, normal to the cavity mode. Additionally, χ controls the degree of elliptic polarization, with $\chi = 0$ yielding linear polarization. The coupling strength g_m and phase ϕ_m discussed in the main text are obtained as $g_m = |G_m|$ and $\phi_m = -\arg\left(G_m\right)$.

Consider the case of vanishing tensor-polarizability $\alpha_t = 0$ and linear polarization of the pump field $\chi = 0$. Then the effective Dicke model is characterized by the coupling strengths

$$g_m = 2E_p E_c\sqrt{\alpha_s^2\cos^2\left(\varphi\right) + \frac{\alpha_v^2 m^2}{4f^2}\sin^2\left(\varphi\right)} \tag{A.9}$$

and the phases

$$\phi_m = -\tan^{-1}\left\{\frac{\alpha_v}{\alpha_s}\frac{m}{2f}\tan(\varphi)\right\} \tag{A.10}$$

Since m only appears quadratically in g_m, it is clear that the coupling strengths are symmetric under swapping of species $m \longleftrightarrow -m$, $g_m = g_{-m}$. Moreover, since inverse tangent is an odd function, it is also clear that the phases are anti-symmetric under swapping of species $m \longleftrightarrow -m$, $\phi_m = -\phi_{-m}$. These are the conditions assumed in the main text.

All other parameters being equal, species with nonzero m interact with the cavity mode with an enhanced strength

$$g_m = g_0\sqrt{1+\left(\frac{\alpha_v}{\alpha_s}\right)^2\frac{m^2}{4f^2}\tan^2(\varphi)} \tag{A.11}$$

where $g_0 = 2E_pE_c\,|\alpha_s\cos(\varphi)|$. In particular, the $m = 0$ species becomes “dark” when the pump and cavity polarization are aligned $\varphi = \pi/2$. Physically, this is because the when $\varphi = \pi/2$ then only the vector and tensor polarizability contribute to the interaction, which are zero for the $m = 0$ species.

In the main text, we primarily study the phase diagram in the theoretically-helpful parameters (g_m, ϕ_m). However, we can also parameterize the coupling strengths g_m and phases ϕ_m as

$$g_m = A_1\,|\cos(\varphi)|\sqrt{1+A_2^2m^2\tan^2(\varphi)} \tag{A.12}$$

$$\phi_m = -\tan^{-1}\{A_2 m\tan(\varphi)\} \tag{A.13}$$

where $A_1 = 2E_pE_c\,|\alpha_s|$ and $A_2 = \alpha_v/2f\alpha_s$. Then we can study the distorted phase diagram in the parameters A_1, controlled by the intensity of the pump field, and φ, controlled by the pump field polarization, for fixed A_2, controlled by the ratio of vector and scalar polarizabilities.

B Derivation of the effective spin-only dynamics

Integrating out the cavity mode in addition to the extra-cavity bath modes, we obtain the Redfield master equation describing the effective dynamics of the spin-only system. The standard procedure is outlined in the following section.

Let H_{SB} be the interaction between the system and the bath in the Schrödinger picture. In the main text, this is the interaction between the spins and the cavity H_{SC}. We consider the cavity as a part of the bath which is described by the Hamiltonian $H_{\text{C}}+H_{\text{CB}}+H_{\text{B}}$ including intra-bath interactions H_{CB}. The time-evolution of the full system-bath density matrix is governed by the von Neumann equation in the interaction picture

$$\dot{\rho}(t) = -i\left[H_{\text{SB}}(t), \rho(t)\right] = \hat{\mathcal{L}}_{\text{SB}}(t)\rho(t) \tag{B.1}$$

defining the Liouvillian superoperator $\hat{\mathcal{L}}_{\text{SB}}(t) = [H_{\text{SB}}(t), \cdot]$ which is generically time-dependent in the interaction picture. We can insert the formal integral solution of Eq. B.1 back into Eq. B.1 to obtain

$$\dot{\rho}(t) = \hat{\mathcal{L}}_{\text{SB}}(t)\rho(0) + \int_0^t ds\,\hat{\mathcal{L}}_{\text{SB}}(t)\hat{\mathcal{L}}_{\text{SB}}(s)\rho(s) \tag{B.2}$$

which is second-order in the system-bath coupling strength.

From this starting point, we would like to obtain a tractable equation of motion for the reduced density matrix of the system $\rho_\mathrm{S}(t) = \mathrm{tr}_\mathrm{B}(\rho(t))$. To do so, we make standard assumptions on the factorization of the density matrix and time-locality of the system-bath interactions [31] which results in the Redfield master equation for the reduced density matrix of the system

$$\dot{\rho}_\mathrm{S}(t) = \int_0^t ds\, \mathrm{tr}_\mathrm{B}\left\{\hat{\mathcal{L}}_\mathrm{SB}(t)\hat{\mathcal{L}}_\mathrm{SB}(t-s)\rho_\mathrm{S}(t)\otimes\rho_\mathrm{B}\right\} \tag{B.3}$$

where ρ_B is (usually) the equilibrium state of the bath. Finally, we assume that the time-scale of the systems dynamics is much longer than the decay of the bath correlation functions allowing us to extend the integration to the interval $[0,\infty]$ [31]. In the remainder of the paper and the main text, we use the term "Redfield master equation" also to refer to this form of the quantum master equation, but before the secular approximation.

In order to convert the Redfield master equation into a more useful more form, we decompose the system-bath interaction H_SB as

$$H_\mathrm{SB} = \sum_k g_k S_k \otimes B_k \tag{B.4}$$

in the Schrödinger picture, where S_k are operators on the system, B_k are operators on the bath, and g_k are the couplings. Then the Redfield master equation becomes

$$\begin{aligned}\dot{\rho}_S(t) = &-\sum_{k,k',\omega,\omega'} g_k g_{k'} e^{i(\omega+\omega')t} \\ &\times\left\{\tilde{C}^{(B)}_{kk'}(\omega',t)\left[\tilde{S}_k(\omega),\tilde{S}_{k'}(\omega')\rho_S(t)\right] + \tilde{C}^{(B)}_{k'k}(-\omega',-t)\left[\tilde{S}_k(\omega),\rho_S(t)\tilde{S}_{k'}(\omega')\right]\right\}\end{aligned} \tag{B.5}$$

where $\tilde{S}_k$ are the Fourier components of the system operators $S_k(t) = \sum_\omega e^{i\omega t}\tilde{S}_k(\omega)$ in the interaction picture, and the bath correlation functions

$$C^{(B)}_{kk'}(t) = \mathrm{tr}_\mathrm{B}(B_k(t)B_{k'}(0)\rho_\mathrm{B}) \tag{B.6}$$

are converted to frequency-space on a finite time-window of length t

$$\tilde{C}^{(B)}_{kk'}(\omega',\pm t) = \int_0^{\pm t} ds\, e^{-i\omega' s} C^{(B)}_{kk'}(s) \tag{B.7}$$

The sign of t is crucial when extending the integration $t\to\infty$.

Expanding the commutators in Eq. B.5 and rearranging terms, we can obtain the quantum master equation in the usual form in terms of a coherent Hamiltonian evolution and dissipative evolution. Additionally, the secular approximation is often used to neglect nonresonant transitions (terms with $\omega+\omega'\neq 0$ in Eq. B.5) induced by the system-bath coupling. However, we keep nonsecular terms in order to capture the superradiant behavior of the Dicke model, as discussed in the main text.

The adjoint Redfield master equation for a generic system operator A is obtained from Eq. B.5 by demanding that the expectation value of A is unchanged between the Schrödinger and Heisenberg pictures [31]. This results in the condition

$$\mathrm{tr}_S\left(A\hat{\mathcal{L}}_\mathrm{eff}\rho_\mathrm{S}(t)\right) = \mathrm{tr}_S\left(\left(\hat{\mathcal{L}}^*_\mathrm{eff}A(t)\right)\rho_\mathrm{S}\right) \tag{B.8}$$

where $\hat{\mathcal{L}}_\mathrm{eff}$ is the effective Liouvillian superoperator governing the time-evolution of the reduced density matrix of the system $\dot{\rho}_\mathrm{S}(t) = \hat{\mathcal{L}}_\mathrm{eff}\rho_\mathrm{S}(t)$ in the Schrödinger picture, as in Eq. B.5, and $\hat{\mathcal{L}}^*_{\text{eff}}$ is the adjoint effective Liouvillian superoperator governing the time-evolution of correlation functions as $d\langle A\rangle/dt = \left\langle \hat{\mathcal{L}}^*_{\text{eff}} A\right\rangle$.

Having discussed general aspects of the derivation of the Redfield master equation, we apply the analysis to the system described in the main text. In particular, we note that generic system-bath interaction H_{SB} used in the derivation is precisely the spin-cavity interaction H_{SC} from the main text. Therefore we have the system operators $S_m = S_1^{(m)}$ and the bath operators $B_m = e^{-i\phi_m} a + e^{i\phi_m} a^\dagger$ with the couplings g_m. The Fourier decomposition of $S_1^{(m)}$ in the interaction picture is simply

$$S_1^{(m)}(t) = \frac{1}{2}\left(e^{-i\epsilon t} S_-^{(m)} + e^{i\epsilon t} S_+^{(m)}\right) \tag{B.9}$$

What remains to be calculated are the bath correlation functions, expanded as

$$\begin{aligned} C^{(B)}_{mm'}(t) = {} & e^{-i(\phi_m+\phi_{m'})}\text{tr}_{\text{B}}\left(a(t)\,a(0)\,\rho_{\text{B}}\right) + e^{i(\phi_m+\phi_{m'})}\text{tr}_{\text{B}}\left(a^\dagger(t)\,a^\dagger(0)\,\rho_{\text{B}}\right) \\ & + e^{-i(\phi_m-\phi_{m'})}\text{tr}_{\text{B}}\left(a(t)\,a^\dagger(0)\,\rho_{\text{B}}\right) + e^{i(\phi_m-\phi_{m'})}\text{tr}_{\text{B}}\left(a^\dagger(t)\,a(0)\,\rho_{\text{B}}\right) \end{aligned} \tag{B.10}$$

Assuming ρ_{B} is an equilibrium thermal state, then we arrive at the standard expression

$$C^{(B)}_{mm'}(t) = \int_{-\infty}^{\infty} \frac{d\omega}{2\pi} J_0^{(B)}(\omega)\left(e^{i(\phi_m-\phi_{m'})}\bar{n}_{\text{eq}}(\omega)\,e^{i\omega s} + e^{-i(\phi_m-\phi_{m'})}\left(\bar{n}_{\text{eq}}(\omega)+1\right)e^{-i\omega s}\right) \tag{B.11}$$

modified due to the phases ϕ_m, where $J_0^{(B)}$ is the zero-temperature spectral density formally given by the expression $J_0^{(B)} = 2\pi\sum_j \left|c_j\right|^2 \delta\left(\omega-\omega_j\right)$ where the bath operator B_m is expanded in the eigenmodes of $H_{\text{C}}+H_{\text{CB}}+H_{\text{B}}$ of energy ω_j with coefficients c_k, and $\bar{n}_{\text{eq}}(\omega)$ is the Bose-Einstein distribution function (at inverse temperature β) giving the thermal occupation of the bath eigenmode of energy ω. In practice, specifying an approximate continuous zero-temperature spectral density enables analytic treatment of the correlation function, taking care to apply the Sokhotski–Plemelj theorem when applicable. In this paper, we assume the spectral density is Lorentzian (Cauchy) with a center frequency given by the cavity mode ω_c and half-width at half-max κ

$$J_0^{(B)} = \frac{2\kappa}{(\omega-\omega_c)^2+\kappa^2} \tag{B.12}$$

which, like the exact form, is normalized to unity. Assuming zero or very low temperature, we obtained

$$C^{(B)}_{mm'}(t) = e^{-i\Delta\phi}e^{-i\omega_c t - i\kappa|t|} \tag{B.13}$$

where $\Delta\phi = \phi_m - \phi_{m'}$ as presented in the main text, and

$$\tilde{C}^{(B)}_{mm'}(\omega,t) = e^{-i\Delta\phi}\left(\frac{1-e^{-i(\omega_c+\omega)t-\kappa t}}{i(\omega_c+\omega)+\kappa}\right) \tag{B.14}$$

$$\lim_{t\to\infty}\tilde{C}^{(B)}_{mm'}(\omega,t) = e^{-i\Delta\phi}\frac{1}{i(\omega_c+\omega)+\kappa} \tag{B.15}$$

$$\tilde{C}^{(B)}_{mm'}(\omega,-t) = e^{-i\Delta\phi}\left(\frac{1-e^{i(\omega_c+\omega)t-\kappa t}}{i(\omega_c+\omega)-\kappa}\right) \tag{B.16}$$

$$\lim_{t\to\infty}\tilde{C}^{(B)}_{mm'}(\omega,-t) = e^{-i\Delta\phi}\frac{1}{i(\omega_c+\omega)-\kappa} \tag{B.17}$$

Substitution of the above results into Eq. B.5 yields Eq. 8 or Eq. B.18, discussed in the following section.

B.1 Alternative form of the spin-only Redfield master equation

As mentioned in the main text, we can transform Eq. 8 into a form which highlights the connection to the mean-field equations of motion Eq. 13. In particular, in terms of the Hermitian $x = 1$, $y = 2$, and $z = 3$ spin operators we have

$$\begin{aligned}\hat{\mathcal{L}}^{*}A = i\,[H_{\mathrm{S}},A] + \sum_{m,m'=-M}^{M}\frac{g_m g_{m'}}{\sqrt{N_m N_{m'}}}\Bigg(\left(\frac{\cos\Delta\phi}{J_1}-\frac{\sin\Delta\phi}{K_1}\right)\left[\left[S_1^{(m)},A\right],S_1^{(m')}\right]\\ +\left(\frac{\cos\Delta\phi}{J_2}-\frac{\sin\Delta\phi}{K_2}\right)\left[\left[S_1^{(m)},A\right],S_2^{(m')}\right]+\left(\frac{\cos\Delta\phi}{K_1}+\frac{\sin\Delta\phi}{J_1}\right)\left\{-i\left[S_1^{(m)},A\right],S_1^{(m')}\right\}\\ +\left(\frac{\cos\Delta\phi}{K_2}+\frac{\sin\Delta\phi}{J_2}\right)\left\{-i\left[S_1^{(m)},A\right],S_2^{(m')}\right\}\Bigg)+\Gamma\sum_{m=-M}^{M}\sum_{j=1}^{N_m}\hat{\mathcal{D}}^{*}\left[s_-^{(m,j)}\right]A\end{aligned} \tag{B.18}$$

with the parameters J_1, J_2, K_1, and K_2 defined in the main text. If A is proportional to a product of k spin operators, then the commutator-commutator terms in Eq. B.18 generically yield terms of the same order as A which are sub-extensive and do not survive in the thermodynamic limit (though they may be significant for finite and small N_m). On the other hand, the anticommutator-commutator terms in Eq. B.18 generically yield symmetrized products of $k+1$ spin operators (up to sub-extensive lower-order corrections) which are significant even in the thermodynamic limit. In the important case when A is a first-order spin operator, the anticommutator-commutator terms in Eq. B.18 yield quadratic nonlinearities, as seen in Eq. 13.

C Exact numerical diagonalization

We compute the exact dynamics of the Lindblad master equation in the fast-cavity limit $\kappa, \omega_c \gg \epsilon$ numerically after exploiting permutation symmetry. As noted in the main text, the density matrix can be decomposed into blocks of fixed spins $(s_i) = (s_{-M}, \ldots, s_M)$ as

$$\rho = \sum_{(s_i)} p_{(s_i)}\rho_{(s_i)} \tag{C.1}$$

$$= \sum_{(s_i)} p_{(s_i)} \sum_{(\mu_i,\mu_i')} p'_{((\mu_i,\mu_i'))}\,|(s_i,\mu_i)\rangle\left\langle(s_i,\mu_i')\right| \tag{C.2}$$

where $p_{(s_i)}$ is the probability of density matrix block $\rho^{(s_i)}$ which can be written explicitly in terms of the probabilities $p'_{((\mu_i,\mu_i'))}$ and the operator basis for fixed (s_i), $|(s_i,\mu_i)\rangle\left\langle(s_i,\mu_i')\right|$. Here, μ_i is used for the magnetic quantum number of species i in order to avoid confusion with the species label m. Then we vectorize the quantum master equation as $|\dot{\rho}\rangle\rangle = \hat{\hat{\mathcal{L}}}|\rho\rangle\rangle$, where $|\rho\rangle\rangle$ is the vectorization of the density matrix ρ and $\hat{\hat{\mathcal{L}}}$ is the vectorization of the Liouvillian superoperator in Lindblad form $\hat{\mathcal{L}}$, a matrix. Using the standard vectorization procedure, the vectorized density matrix [32] is

$$|\rho\rangle\rangle = \sum_{(s_i)} p_{(s_i)} \sum_{(\mu_i,\mu_i')} p'_{((\mu_i,\mu_i'))}\left|(s_i,\mu_i,\mu_i')\right\rangle\rangle \tag{C.3}$$

For the vectorized Liouvillian superoperator in Lindblad form, we generalize the expressions in Ref. [50] for off-diagonal dissipative processes (coherence between decay and pumping) and multiple species. The matrix elements are then

$$\hat{\hat{\mathcal{L}}} = \sum_{\substack{(s_i,\mu_i,\mu_i') \\ (t_i,\nu_i,\nu_i')}} \mathcal{L}_{((s_i,\mu_i,\mu_i'),(t_i,\nu_i,\nu_i'))} \big|(s_i,\mu_i,\mu_i')\rangle\!\rangle \langle\!\langle(t_i,\nu_i,\nu_i')\big| \tag{C.4}$$

with explicit expressions for the matrix elements $\mathcal{L}_{((s_i,\mu_i,\mu_i'),(t_i,\nu_i,\nu_i'))}$ left out of this section for brevity. However, due to the nature of the Dicke coupling, excitations must be exchanged in pairs, thus constraining the matrix elements off-diagonal in μ_i, μ_i', ν_i, and ν_i'. Additionally, the quantum jumps from single-particle incoherent decay (as well as single-particle dephasing and single-particle incoherent pumping) can only lead to coupling between total-spin manifolds satisfying $s_i = t_i$ or $s_i = t_i \pm 1$.

To visualize the density matrix, we first calculate the reduced density matrix of each species

$$\rho^{(m)} = \mathrm{tr}_{m' \neq m}(\rho) \tag{C.5}$$

then write the reduced density matrix in block-diagonal form

$$\rho^{(m)} = \sum_{s_m} p_{s_m}^{(m)} \rho^{(m,s_m)} \tag{C.6}$$

Similar to the full density matrix, $p_{s_m}^{(m)}$ is the probability of density matrix block $\rho^{(m,s_m)}$. Next, we extract the Wigner (quasi-probability) distribution for species m of fixed spin s_m as

$$W_{s_m}^{(m)}(\vartheta,\varphi) = \mathrm{tr}\left(\mathcal{W}_{s_m}(\vartheta,\varphi)\,\rho^{(m,s_m)}\right) \tag{C.7}$$

where

$$\mathcal{W}_s(\vartheta,\varphi) = \sqrt{\frac{4\pi}{2s+1}} \sum_{\lambda=0}^{2s} \sum_{\mu=-\lambda}^{\lambda} Y_{\lambda\mu}(\vartheta,\varphi)\, T_{\lambda\mu}^{(s)\dagger} \tag{C.8}$$

is the Wigner (operator) kernel, $Y_{\lambda\mu}$ are spherical harmonics, and $T_{\lambda\mu}^{(m,s)}$ are irreducible tensor operators [52]. We note that the Wigner kernal has the following properties

$$\mathcal{W}_s(\vartheta,\varphi) = \mathcal{W}_s(\vartheta,\varphi)^\dagger \tag{C.9}$$

$$\mathrm{tr}(\mathcal{W}_s(\vartheta,\varphi)) = 1 \tag{C.10}$$

$$\frac{2s+1}{4\pi} \int d\Omega\, \mathcal{W}_s(\vartheta,\varphi) = 1 \tag{C.11}$$

Since the Wigner kernal is Hermitian (as is the density matrix), the Wigner distribution is real. Moreover, it can be normalized, though permitting negative values. Lastly, we average over the allowed values of spin s_m to obtain the spin-averaged Wigner distribution.

$$W^{(m)}(\vartheta,\varphi) = \sum_{s_m} p_{s_m} \left(\frac{2s_m+1}{4\pi}\right) W_{s_m}^{(m)}(\vartheta,\varphi) \tag{C.12}$$

If the reduced density matrix $\rho^{(m)}$ is proportional to the identity, i.e. a completely mixed state, then the Wigner distribution for species m of fixed spin s_m is simply

$$W_{s_m}^{(m)}(\vartheta,\varphi) = \frac{1}{2s_m+1} \tag{C.13}$$

and the spin-averaged Wigner distribution is $W^{(m)}(\vartheta,\varphi) = 1/4\pi$. This value $1/4\pi \approx 0.08$ is used in the main text as a reference.

References

[1] A. Ivlev, J. Bartnick, M. Heinen, C.-R. Du, V. Nosenko and H. Löwen, *Statistical mechanics where Newton's Third Law is broken*, Physical Review X **5**(1), 011035 (2015), doi:10.1103/PhysRevX.5.011035.

[2] M. Fruchart, R. Hanai, P. B. Littlewood and V. Vitelli, *Non-reciprocal phase transitions*, Nature **592**(7854), 363 (2021), doi:10.1038/s41586-021-03375-9.

[3] T. Prosen, *PT-Symmetric quantum Liouvillean dynamics*, Physical Review Letters **109**(9), 090404 (2012), doi:10.1103/PhysRevLett.109.090404.

[4] J. Huber, P. Kirton, S. Rotter and P. Rabl, *Emergence of PT-symmetry breaking in open quantum systems*, SciPost Physics **9**(4), 052 (2020), doi:10.21468/SciPostPhys.9.4.052.

[5] F. Minganti, A. Miranowicz, R. W. Chhajlany and F. Nori, *Quantum exceptional points of non-Hermitian Hamiltonians and Liouvillians: The effects of quantum jumps*, Physical Review A **100**(6), 062131 (2019), doi:10.1103/PhysRevA.100.062131.

[6] E. I. R. Chiacchio, A. Nunnenkamp and M. Brunelli, *Nonreciprocal Dicke model*, Physical Review Letters **131**(11), 113602 (2023), doi:10.1103/PhysRevLett.131.113602.

[7] R. Hanai, D. Ootsuki and R. Tazai, *Photoinduced non-reciprocal magnetism*, ArXiv:2406.05957 [cond-mat] (2024).

[8] T. Nadolny, C. Bruder and M. Brunelli, *Nonreciprocal synchronization of active quantum spins*, Physical Review X **15**(1), 011010 (2025), doi:10.1103/PhysRevX.15.011010.

[9] S. Yao and Z. Wang, *Edge states and topological invariants of non-Hermitian systems*, Physical Review Letters **121**(8), 086803 (2018), doi:10.1103/PhysRevLett.121.086803.

[10] X. Zhang, T. Zhang, M.-H. Lu and Y.-F. Chen, *A review on non-Hermitian skin effect*, Advances in Physics: X **7**(1), 2109431 (2022), doi:10.1080/23746149.2022.2109431.

[11] R. H. Dicke, *Coherence in spontaneous radiation processes*, Physical Review **93**(1), 99 (1954), doi:10.1103/PhysRev.93.99.

[12] K. Hepp and E. H. Lieb, *Equilibrium statistical mechanics of matter interacting with the quantized radiation field*, Physical Review A **8**(5), 2517 (1973), doi:10.1103/PhysRevA.8.2517.

[13] K. Hepp and E. H. Lieb, *On the superradiant phase transition for molecules in a quantized radiation field: the dicke maser model*, Annals of Physics **76**(2), 360 (1973), doi:10.1016/0003-4916(73)90039-0.

[14] F. Damanet, A. J. Daley and J. Keeling, *Atom-only descriptions of the driven-dissipative Dicke model*, Physical Review A **99**(3), 033845 (2019), doi:10.1103/PhysRevA.99.033845.

[15] D. A. Paz and M. F. Maghrebi, *Driven-dissipative Ising model: An exact field-theoretical analysis*, Physical Review A **104**(2), 023713 (2021), doi:10.1103/PhysRevA.104.023713.

[16] P. Kirton, M. M. Roses, J. Keeling and E. G. Dalla Torre, *Introduction to the Dicke model: From equilibrium to nonequilibrium, and vice versa*, Advanced Quantum Technologies **2**(1-2), 1800043 (2019), doi:10.1002/qute.201800043.

[17] P. Domokos and H. Ritsch, *Collective cooling and self-organization of atoms in a cavity*, Physical Review Letters **89**(25), 253003 (2002), doi:10.1103/PhysRevLett.89.253003.

[18] A. T. Black, H. W. Chan and V. Vuletić, *Observation of collective friction forces due to spatial self-organization of atoms: From Rayleigh to Bragg scattering*, Physical Review Letters **91**(20), 203001 (2003), doi:10.1103/PhysRevLett.91.203001.

[19] K. Baumann, C. Guerlin, F. Brennecke and T. Esslinger, *Dicke quantum phase transition with a superfluid gas in an optical cavity*, Nature **464**(7293), 1301 (2010), doi:10.1038/nature09009.

[20] D. Nagy, G. Kónya, G. Szirmai and P. Domokos, *Dicke-model phase transition in the quantum motion of a Bose-Einstein condensate in an optical cavity*, Physical Review Letters **104**(13), 130401 (2010), doi:10.1103/PhysRevLett.104.130401.

[21] J. Léonard, A. Morales, P. Zupancic, T. Esslinger and T. Donner, *Supersolid formation in a quantum gas breaking a continuous translational symmetry*, Nature **543**(7643), 87 (2017), doi:10.1038/nature21067.

[22] M. Landini, N. Dogra, K. Kroeger, L. Hruby, T. Donner and T. Esslinger, *Formation of a spin texture in a quantum gas coupled to a cavity*, Physical Review Letters **120**(22), 223602 (2018), doi:10.1103/PhysRevLett.120.223602.

[23] N. Dogra, M. Landini, K. Kroeger, L. Hruby, T. Donner and T. Esslinger, *Dissipation-induced structural instability and chiral dynamics in a quantum gas*, Science **366**(6472), 1496 (2019), doi:10.1126/science.aaw4465.

[24] M. J. Bhaseen, J. Mayoh, B. D. Simons and J. Keeling, *Dynamics of nonequilibrium Dicke models*, Physical Review A **85**(1), 013817 (2012), doi:10.1103/PhysRevA.85.013817.

[25] P. Kirton and J. Keeling, *Superradiant and lasing states in driven-dissipative Dicke models*, New Journal of Physics **20**(1), 015009 (2018), doi:10.1088/1367-2630/aaa11d.

[26] F. Carollo and I. Lesanovsky, *Exactness of mean-field equations for open Dicke models with an application to pattern retrieval dynamics*, Physical Review Letters **126**(23), 230601 (2021), doi:10.1103/PhysRevLett.126.230601.

[27] R. Hanai, A. Edelman, Y. Ohashi and P. B. Littlewood, *Non-Hermitian phase transition from a polariton Bose-Einstein condensate to a photon laser*, Physical Review Letters **122**(18), 185301 (2019), doi:10.1103/PhysRevLett.122.185301.

[28] H. Keßler, J. G. Cosme, M. Hemmerling, L. Mathey and A. Hemmerich, *Emergent limit cycles and time crystal dynamics in an atom-cavity system*, Physical Review A **99**(5), 053605 (2019), doi:10.1103/PhysRevA.99.053605.

[29] E. R. Chiacchio and A. Nunnenkamp, *Dissipation-induced instabilities of a spinor Bose-Einstein condensate inside an optical cavity*, Physical Review Letters **122**(19), 193605 (2019), doi:10.1103/PhysRevLett.122.193605.

[30] A. Clerk, *Introduction to quantum non-reciprocal interactions: from non-Hermitian Hamiltonians to quantum master equations and quantum feedforward schemes*, SciPost Physics Lecture Notes p. 44 (2022), doi:10.21468/SciPostPhysLectNotes.44.

[31] H.-P. Breuer and F. Petruccione, *The Theory of Open Quantum Systems*, Oxford University Press, Oxford ; New York, ISBN 978-0-19-852063-4, OCLC: ocm49872077 (2002).

[32] R. Fazio, J. Keeling, L. Mazza and M. Schirò, *Many-Body Open Quantum Systems*, doi:10.48550/arXiv.2409.10300, ArXiv:2409.10300 [quant-ph] (2024).

[33] B. Buca and D. Jaksch, *Dissipation induced nonstationarity in a quantum gas*, Physical Review Letters **123**(26), 260401 (2019), doi:10.1103/PhysRevLett.123.260401.

[34] P. Kirton and J. Keeling, *Suppressing and restoring the Dicke superradiance transition by dephasing and decay*, Physical Review Letters **118**(12), 123602 (2017), doi:10.1103/PhysRevLett.118.123602.

[35] E. G. D. Torre, S. Diehl, M. D. Lukin, S. Sachdev and P. Strack, *Keldysh approach for nonequilibrium phase transitions in quantum optics: Beyond the Dicke model in optical cavities*, Physical Review A **87**(2), 023831 (2013), doi:10.1103/PhysRevA.87.023831.

[36] E. G. D. Torre, Y. Shchadilova, E. Y. Wilner, M. D. Lukin and E. Demler, *Dicke phase transition without total spin conservation*, Physical Review A **94**(6), 061802 (2016), doi:10.1103/PhysRevA.94.061802.

[37] J. Gelhausen, M. Buchhold and P. Strack, *Many-body quantum optics with decaying atomic spin states: (γ , κ) Dicke model*, Physical Review A **95**(6), 063824 (2017), doi:10.1103/PhysRevA.95.063824.

[38] J. Gelhausen and M. Buchhold, *Dissipative Dicke model with collective atomic decay: Bistability, noise-driven activation, and the nonthermal first-order superradiance transition*, Physical Review A **97**(2), 023807 (2018), doi:10.1103/PhysRevA.97.023807.

[39] L. A. Correa and J. Glatthard, *Potential renormalisation, Lamb shift and mean-force Gibbs state—to shift or not to shift?*, doi:10.48550/arXiv.2305.08941, ArXiv:2305.08941 [quant-ph] (2024).

[40] P. R. Eastham, P. Kirton, H. M. Cammack, B. W. Lovett and J. Keeling, *Bath-induced coherence and the secular approximation*, Physical Review A **94**(1), 012110 (2016), doi:10.1103/PhysRevA.94.012110.

[41] B. Buča and T. Prosen, *A note on symmetry reductions of the Lindblad equation: Transport in constrained open spin chains*, New Journal of Physics **14**(7), 073007 (2012), doi:10.1088/1367-2630/14/7/073007.

[42] F. Mivehvar, *Conventional and unconventional Dicke models: Multistabilities and nonequilibrium dynamics*, Physical Review Letters **132**(7), 073602 (2024), doi:10.1103/PhysRevLett.132.073602.

[43] Y. Nakanishi, R. Hanai and T. Sasamoto, *Continuous time crystals as a PT symmetric state and the emergence of critical exceptional points*, doi:10.48550/arXiv.2406.09018, ArXiv:2406.09018 [quant-ph] (2025).

[44] M. Xu, D. A. Tieri and M. J. Holland, *Simulating open quantum systems by applying SU(4) to quantum master equations*, Physical Review A **87**(6), 062101 (2013), doi:10.1103/PhysRevA.87.062101.

[45] S. Hartmann, *Generalized Dicke states*, doi:10.48550/arXiv.1201.1732, ArXiv:1201.1732 [quant-ph] (2016).

[46] J. Keeling, M. J. Bhaseen and B. D. Simons, *Collective dynamics of Bose-Einstein condensates in optical cavities*, Physical Review Letters **105**(4), 043001 (2010), doi:10.1103/PhysRevLett.105.043001.

[47] M. Soriente, T. Donner, R. Chitra and O. Zilberberg, *Dissipation-induced anomalous multicritical phenomena*, Physical Review Letters **120**(18), 183603 (2018), doi:10.1103/PhysRevLett.120.183603.

[48] J. Hannukainen and J. Larson, *Dissipation-driven quantum phase transitions and symmetry breaking*, Physical Review A **98**(4), 042113 (2018), doi:10.1103/PhysRevA.98.042113.

[49] F. Minganti, A. Biella, N. Bartolo and C. Ciuti, *Spectral theory of Liouvillians for dissipative phase transitions*, Physical Review A **98**(4), 042118 (2018), doi:10.1103/PhysRevA.98.042118.

[50] N. Shammah, S. Ahmed, N. Lambert, S. De Liberato and F. Nori, *Open quantum systems with local and collective incoherent processes: Efficient numerical simulations using permutational invariance*, Physical Review A **98**(6), 063815 (2018), doi:10.1103/PhysRevA.98.063815.

[51] B. A. Chase and J. M. Geremia, *Collective processes of an ensemble of spin-1/2 particles*, Physical Review A **78**(5), 052101 (2008), doi:10.1103/PhysRevA.78.052101.

[52] A. B. Klimov and S. M. Chumakov, *A Group-Theoretical Approach to Quantum Optics: Models of Atom-Field Interactions*, WILEY-VCH Verlag GmbH & Co., ISBN 978-3-527-40879-5 (2009).

[53] S. Dutta, S. Zhang and M. Haque, *Quantum origin of limit cycles, fixed points, and critical slowing down*, Physical Review Letters **134**(5), 050407 (2025), doi:10.1103/PhysRevLett.134.050407.

[54] W. Happer, *Optical Pumping*, Reviews of Modern Physics **44**(2), 169 (1972), doi:10.1103/RevModPhys.44.169.

[55] F. Le Kien, P. Schneeweiss and A. Rauschenbeutel, *Dynamical polarizability of atoms in arbitrary light fields: general theory and application to cesium*, The European Physical Journal D **67**(5), 92 (2013), doi:10.1140/epjd/e2013-30729-x.

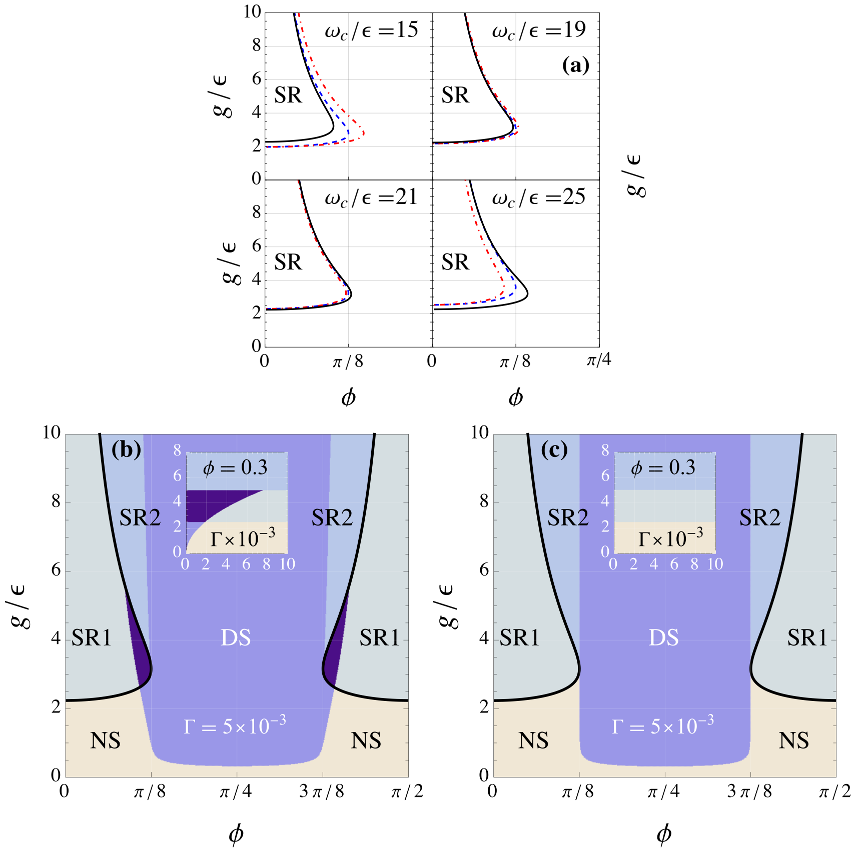

Figure 3: Comparison of the linear stability analyses of the normal state fixed-point $\boldsymbol{\tau}_{\mathrm{ns}}$ for a two-species model. (a) Boundary of the superradiant phase as indicated by the appearance of a pair of stable fixed-points with $\tau_3^{(m)} > 0$ breaking the SR parity symmetry (see text). The mean-field prediction Eq. 13 (dashed blue) derived from the Redfield master equation is compared to the mean-field prediction in the fast-cavity limit $\kappa, \omega_c \gg \epsilon$ after semiclassical adiabatic elimination Eq. 18 (dot-dashed red), as well as the mean-field equations following from Eq. 7 (solid black) which retain the cavity mode. For $\omega_c \approx \kappa$, the boundaries are nearly coincident, a special point discussed in the main text and also indicated in Fig. 2. In the limit $\kappa \to \infty$, the region vanishes in the parameter ϕ. (b, c) Even with the cavity decay rate and cavity energy tuned to $\omega_c/\epsilon = \kappa/\epsilon = 20$, the linear stability analyses of the normal state fixed-point $\boldsymbol{\tau}_{\mathrm{ns}}$ differ qualitatively. (b) Linear stability analysis Eq. 16 derived from the Redfield master equation providing local information on the stability of $\boldsymbol{\tau}_{\mathrm{ns}}$. (c) Linear stability analysis in the fast-cavity limit $\kappa, \omega_c \gg \epsilon$ after semiclassical adiabatic elimination, Eq. 20 providing local information on the stability of $\boldsymbol{\tau}_{\mathrm{ns}}$. In the main figures, the phase ϕ and the coupling strength g/ϵ are varied while the single-particle incoherent decay rate $\Gamma/\epsilon = 5 \times 10^{-3}$ is fixed; in the inset the single-particle incoherent decay rate Γ/ϵ and the coupling strength g/ϵ are varied while the phase $\phi = 0.3$ is fixed. Color indicates the stability or type of instability of the normal state fixed-point $\boldsymbol{\tau}_{\mathrm{ns}}$: Stable ("NS," tan), unstable with a pair of complex-conjugate eigenvalues with positive real-part ("DS," blue), unstable with a single real eigenvalue ("SR1," green), unstable with two real eigenvalues ("SR2," light-blue), unstable with a real eigenvalue and a pair of complex-conjugate eigenvalues with positive real-part (unlabeled, dark-purple).

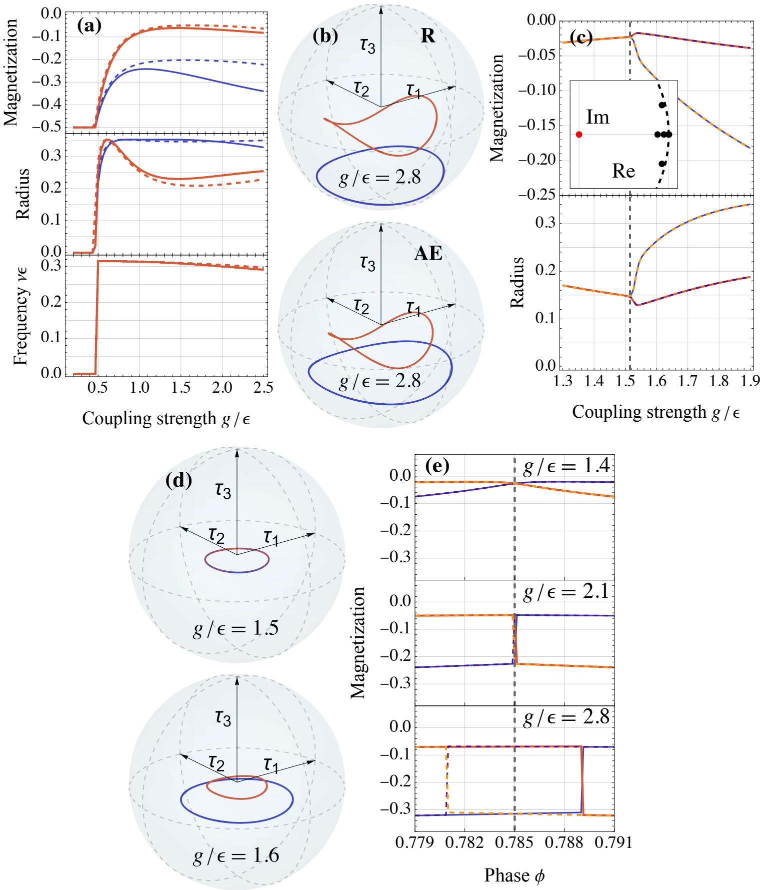

Figure 4: Analysis of the dynamical limit-cycle phase for a two-species model. (a) Characterization of the limit-cycle state for increasing coupling strength g/ϵ. The time-averaged magnetization (see text) of the limit-cycle state is plotted alongside the time-averaged oscillation radius (see text) as well as the oscillation frequency (largest Fourier component) for Eq. 13 (solid) and Eq. 18 (dashed) and each species, species 1 ($m = +1$, blue) and species 2 ($m = -1$, red). The phase $\phi = \pi/4 - 0.1 \approx 0.68$ is slightly tuned away from $\phi = \pi/4$ to differentiate the species (see (c-e)). (b) Example of the limit-cycle state in the Bloch sphere at the point $g/\epsilon = 2.8$ using Eq. 13 (upper) and Eq. 18 (lower) and separating each species, species 1 ($m = +1$, blue) and species 2 ($m = -1$, red). (c) The time-averaged magnetization of the limit-cycle state is plotted alongside the time-averaged oscillation radius for each species 1 ($m = +1$, blue) and 2 ($m = -1$, red) and symmetric (solid) and anti-symmetric (dashed) initial conditions as a function of the coupling strength g/ϵ within the dynamical limit-cycle phase (using Eq. 13). At $g/\epsilon \approx 1.515$ the system reaches a codimension-two exceptional point and the formerly coincident limit-cycles for each species differentiate. (Inset) Floquet multipliers inside the complex unit circle (dashed, center at red point) calculated as the eigenvalues of the monodromy matrix at the transition point (with coincident points at unity 1). (d) Example of the limit-cycle state in the Bloch sphere below the exceptional point $g/\epsilon = 1.5$ (upper) and above the exceptional point $g/\epsilon = 1.6$ (lower). (e) Tuning the “chirality breaking” parameter ϕ uncovers a narrow region about $\phi = \pi/4$ exhibiting hysteresis, growing wider for increasing coupling strength g/ϵ. Symmetric initial conditions (solid) and anti-symmetric initial conditions (dashed) persist on different sides of the line $\phi = \pi/4$ (gray). All plots use the parameters $\kappa/\epsilon = 20$ and $\omega_c/\epsilon = 20$ with (a-b) using $\Gamma/\epsilon = 1 \times 10^{-2}$ and (c-e) using $\Gamma/\epsilon = 5 \times 10^{-3}\epsilon$.

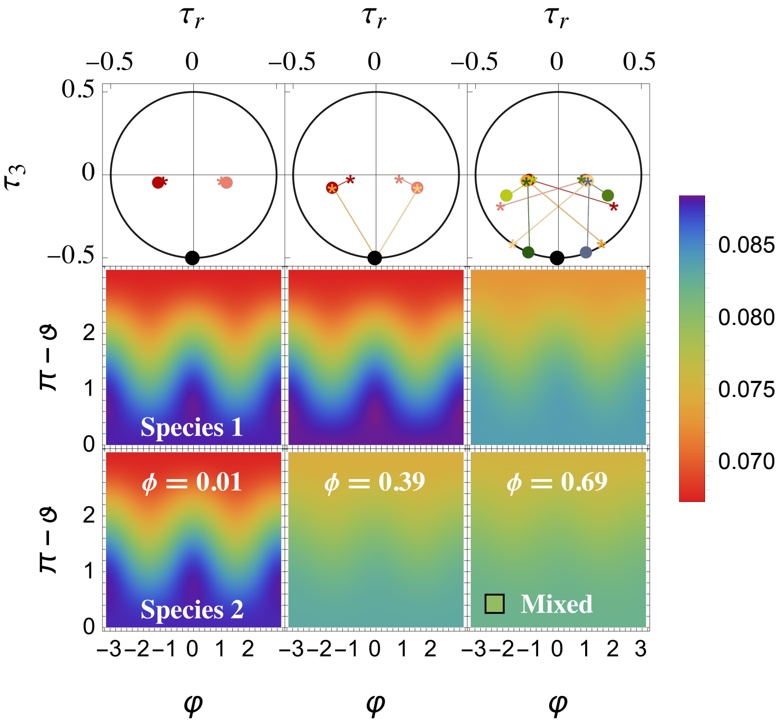

Figure 5: Superradiant steady-states in the fast-cavity limit $\kappa, \omega_c \gg \epsilon$ for various phases $\phi = 0.01$, $\pi/8 \approx 0.39$, and $\pi/4 - 0.1 \approx 0.69$ and fixed coupling strength $g/\epsilon = 8$. (a) The mean-field equations (top row) Eq. 18 yield three fixed-point solutions (two stable) for $\phi = 0.01$, five fixed-point solutions (two stable) for $\pi/8$, and nine fixed-point solutions (four stable) for $\pi/4 - 0.1$, distinguished by color, which lie in the plane defined by the normal $(\cos\beta, \sin\beta, 0)$ with $\beta = \tan^{-1}(-\Gamma/\epsilon) + \pi/2$ (see text). Species 1 is indicated by filled circles while species 2 is indicated by stars, and the two are connected by lines. For a finite-sized system (middle and bottom row) we visualize the density matrix via the spin-averaged Wigner distribution $W^{(m)}(\vartheta, \varphi)$, where ϑ is the polar angle and φ the azimuthal angle, for species 1 ($m = +1$, middle row) and species 2 ($m = -1$, bottom row), each with 6 particles. The value of the spin-averaged Wigner distribution is indicated by the color and colorbar, with $1/4\pi \approx 0.08$ (green) indicating the completely mixed state for reference. For $\phi = 0.01$, the steady-states of each species are nearly identical, while for $\phi = \pi/8$ species 2 experiences dephasing. At $\phi = \pi/4 - 0.1$ species 1 also experiences dephasing as bipartite parity symmetry is nearly restored. We find a unique steady-state despite the change in the number of mean-field fixed-points. All plots use the parameters $\Gamma/\epsilon = 5 \times 10^{-3}$, $\kappa/\epsilon = 20$, and $\omega_c/\epsilon = 20$, as in Fig. 6.

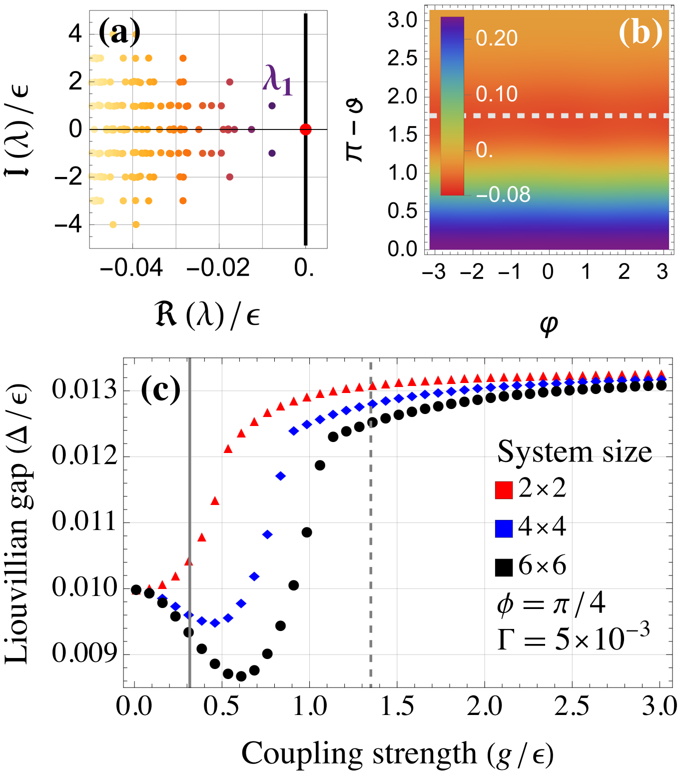

Figure 6: Signatures of the dynamical limit-cycle phase in a finite system in the fast-cavity limit $\kappa, \omega_c \gg \epsilon$. (a) Example spectrum of the Liouvillian in Lindblad form Eq. 12 near the steady-state eigenvalue $\lambda_0 = 0$ at coupling strength $g/\epsilon = 1.35$ and phase $\phi = \pi/4$. (b) Spin-averaged Wigner distribution for species 1 ($m = +1$) $W^{(1)}(\vartheta, \varphi)$, where ϑ is the polar angle and φ the azimuthal angle, of the eigenmatrix corresponding to eigenvalue λ_1 (see text) in Fig. 6a. There is a (negative) concentration of quasi-probability around the latitude $\pi - \vartheta$ of the mean-field limit-cycle (dashed gray), comparable to the mean-field limit-cycle in the top panel of Fig. 4d. Both (a) and (b) use 6 particles in each species and correspond to the dashed gray line in (c). (c) Liouvillian gap for various system sizes as a function of the coupling strength g/ϵ at fixed phase $\phi = \pi/4$. At small coupling strength, the gap is set by a pair of spiraling complex conjugate eigenvalues with nonzero imaginary part, whereas at larger coupling strengths, the gap is set by a decaying real eigenvalue. As the system size increases, the Liouvillian gap begins to decrease towards the mean-field instability (gray solid line). All plots use the parameters $\Gamma/\epsilon = 5 \times 10^{-3}$, $\kappa/\epsilon = 20$, and $\omega_c/\epsilon = 20$, as in Fig. 5.